Daval, D., Hellmann, R., Saldi, G. D., Wirth, R., Knauss, K. G. (2013): Linking nm-scale measurements of the anisotropy of silicate surface reactivity to macroscopic dissolution rate laws: New insights based on diopside. - Geochimica et Cosmochimica Acta, 107, 121-134

DOI: 10.1016/j.gca.2012.12.045

Linking nm-scale measurements of the anisotropy of silicate surface reactivity to macroscopic dissolution rate laws: new insights based on diopside

Damien Daval[a,b*], Roland Hellmann[c], Giuseppe D. Saldi[a], Richard Wirth[d], Kevin G. Knauss[a]

[a] Earth Sciences Division, Lawrence Berkeley National Laboratory, MS 90R-1116, 1 Cyclotron Road, Berkeley, CA 94720, USA

[b] Laboratoire d'Hydrologie et de Géochimie de Strasbourg, Université de Strasbourg /EOST-CNRS UMR 7517, 1 Rue Blessig, 67084 Strasbourg, France

[c] Institute for Earth Sciences ISTerre, Université de Grenoble 1, CNRS, Observatoire des Sciences de l'Univers à Grenoble, 38041, Grenoble, France

[d] GFZ German Research Centre for Geosciences, Telegrafenberg, 14473 Potsdam, Germany

[*]corresponding author: ddaval@unistra.fr (D. Daval)

Tel: +33 (0)3 68 85 05 56; Fax: +33(0)3 68 85 04 02

Abstract

The interfacial zone between a bulk fluid and a mineral surface is where all exchange of matter and energy occurs during chemical weathering. However, our knowledge is still limited with respect to understanding where and how the rate-determining dissolution reactions take place. A complicating factor is the commonplace formation of amorphous Si-rich surface layers (ASSL), which may hinder contact between the fluid and the mineral surface. To address the role of ASSL, we investigated the dissolution of a common silicate (diopside), and related the bulk dissolution rate with the nanoscale dissolution rate and surface chemistry of its individual prevalent faces. While ASSL were evidenced on all of the investigated faces, only those formed on (110) and $(1\bar{1}0)$ were passivating, thereby controlling the reactivity of the underlying faces. The (110) and $(1\bar{1}0)$ faces intersect the highest density of Mg-O-Si and Fe-O-Si bonds, and this specificity may explain the passivating behavior of the corresponding ASSL. Moreover, we evidenced an inverse relation between aqueous silica concentration and the bulk dissolution rate of crushed diopside grains, which suggest that the (110) and $(1\bar{1}0)$ faces are predominant in a powder. By considering ASSL as a separate phase that can control silicate dissolution rates, extrapolated laboratory-based rates at conditions relevant to the field can be lowered by up to several orders of magnitude, thereby decreasing the large gap between laboratory and natural rates. This has important implications for more accurately modeling chemical weathering reactions, so important today for the C cycle and CO_2 sequestration.

Keywords: dissolution kinetics; chemical weathering; passivation; dissolution anisotropy; fluid/silicate interfaces.

1. Introduction

The chemical weathering of silicate materials plays a central role in many major engineering, environmental, and Earth science processes. Whether it determines the rates of denudation and soil formation (Goddéris et al., 2010), CO_2 uptake and its impact on climate change (Le Hir et al., 2008; Beaulieu et al., 2012), hydrothermal circulation (Fritz et al., 2010), durability of radioactive waste confinement glasses (Frugier et al., 2008; Cailleteau et al., 2008) or geological sequestration of CO_2 (Knauss et al., 2005), the same strategy is commonly applied for determining the long term evolution of fluid-rock interactions. This strategy relies on the experimental determination of the influence of a few parameters (mainly pH, temperature (*T*), ionic strength, and concentration of organic ligands) on the dissolution rate of single mineral powders in chemostats, almost always at far-from-equilibrium conditions. The derived kinetic rate laws are subsequently implemented into reactive transport codes (e.g. Knauss et al., 2005; Goddéris et al., 2010). However, the utility of such laws to predict the rates of the abovementioned processes has been questioned for more than 20 years: it is well known that laboratory-based rates can be up to 5 orders of magnitude greater than those measured in the field, casting doubt both on the usefulness of laboratory rates and on the accuracy of reactive transport simulations (White et al., 1996; White and Brantley, 2003; Maher et al., 2004). Despite the emergence of some promising propositions to bridge the gap between laboratory and field measurements (e.g. Nugent et al., 1998; Lasaga and Lüttge, 2001; Arvidson and Lüttge, 2010; Maher, 2010; see detailed discussions in e.g. White and Brantley, 2003; Zhu, 2005), and aside from a limited number of studies which managed to reconcile experimental and field data at specific sites (e.g. Maher et al., 2009), upscaling laboratory results to the field essentially remains an elusive goal.

Addressing this challenge requires an in-depth understanding of silicate reactivity and the underlying nm-scale processes. A key parameter arises from the detailed investigation of weathered silicate surfaces. Hellmann et al. (2012) have recently extended more than 40 years of direct and indirect observations (e.g. Luce et al., 1972; Petit et al. 1987) by demonstrating that regardless of the reaction conditions (fluid composition, *T*, reaction duration and location (i.e. field or laboratory), mineral chemistry and structure, presence of biota), nm-thick amorphous surface altered layers enriched in silica were generally found to have formed on weathered silicate mineral surfaces (note however that the question as to whether or not the formation of such layers is ubiquitous remains open -see e.g. the work by Lee et al. (2008), which failed to find amorphous layers on weathered feldspars in spite of the use of state-of-the-art microscopic techniques). Therefore, as previously pointed out by e.g., Jordan et al. (1999) or Zhu et al. (2006), the basic question that needs to be addressed is: which part of the interfacial zone, defined as the chemically and structurally modified entity between the pristine mineral surface and the bulk fluid, ultimately controls the dissolution rate? The two candidates for answering this question are (a) the inner interface, defined as the boundary between the pristine mineral and the amorphous silica-rich surface layer (hereafter referred to as: ASSL), (b) the outer interface, where the bulk fluid contacts the ASSL. If the ASSL are not passivating, the inner interface will control the kinetics, and conversely, if they are passivating (i.e. totally non-permeable), the outer interface hinders access of the bulk fluid to the unaltered mineral surface, and thereby will control the dissolution process. Both cases have been reported for silicate glasses and minerals (e.g. Jordan et al., 1999; Daval et al., 2009a, b; Geisler et al., 2010; Hellmann et al., 2012 vs. Daux et al., 1997; Berger et al., 2002; Daval et al., 2011). In addition, the presence of passivating ASSL has not yet been integrated in current reactive transport codes. This has important consequences because it can lead to a dramatic overestimation of dissolution rates, even in simple batch experiments (Daval et al.,

2011). The quantitative recognition of the effects of passivation shows promise as a means for reconciling field and laboratory chemical weathering rates.

In the present study, we provide a detailed investigation of the face-specific dissolution of a common silicate mineral (diopside) and combine these results with macroscopic measurements of bulk diopside dissolution rates to shed light on key parameters that render certain ASSL passivating. Quite surprisingly, the results described below show that the passivating properties of ASSL are face-specific. This finding has important consequences on our ability to accurately model the kinetics of fluid-rock interactions, as well as the interpretation of experimental mineral dissolution results determined in the laboratory.

2. Materials and methods

The present study consists of two independent series of experiments aiming at investigating the effect of SiO_2(aq) concentrations on diopside dissolution rates (R_{Di}), both on crushed grains at the macro-scale, and on selected faces at the nano-scale. The starting materials are cm-sized gems coming from Mererani (Tanzania), and were previously described in Daval et al. (2010). Based on electron microprobe analyses, the chemical composition of the diopside used in this study has the following composition: $Ca_{1.01}Mg_{0.96}Fe_{0.05}Si_{1.98}O_6$, in close agreement with that reported in Daval et al. (2010).

2.1 Bulk dissolution experiments on diopside powders in mixed-flow reactors (MFR)

Samples were initially crushed, sieved to recover the 300-500 µm-sized fraction, and ultrasonically washed in absolute ethanol following the procedure described in Daval et al. (2010). The measured Kr BET specific surface area was 0.028 $m^2.g^{-1}$. The experiments were conducted in a MFR system, using the exact same set-up as in Daval et al. (2010). In this previous study, a rate plateau was evidenced as long as the Gibbs free energy with respect to diopside dissolution (ΔG_r(Di)) was below -76 $kJ.mol^{-1}$. Consequently, to single out the

intrinsic effect of [SiO_2(aq)] only, all experiments of the present study were conducted at conditions where R_{Di} is ΔG_r(Di)-independent (for all experiments, ΔG_r(Di) ≤ -89 kJ.mol^{-1}). Consistent with Daval et al. (2010), the experiments were carried out at 90 °C and at 2 MPa fluid pressure, at $pH_{(90°C)}$ close to 5 (4.97 ± 0.04). The input solutions contained an acetate pH buffer (6.4 mM sodium acetate and 5 mM acetic acid; see Daval et al., 2010 for details).

If the Si-rich layers which form on diopside are passivating, R_{Di} should exhibit a strong dependence on [SiO_2(aq)]. Assessing this point was performed by varying the inlet concentration of SiO_2(aq) (by adding variable amounts of sodium metasilicate), with all of the other experimental parameters (sample mass and grain size, flow rate, reaction time, pH) remaining roughly constant from one run to the other. The pH of the input and output solutions was measured periodically. The *in situ* pH and saturation indices of the solution were calculated using the CHESS code (van der Lee and de Windt, 2002), based on the EQ3/6 database (see Daval et al., 2010 for details). Activity coefficients for aqueous species were calculated using the Davies equation. The ionic strength of the solutions was between 7 and 11 mmol.l^{-1}. The inlet and outlet concentrations of dissolved cations (Si, Ca, Mg) were measured by ICP-OES (Varian 720-ES). The steady-state conditions were assumed when the following two conditions were verified: (1) the length of the run was long enough to ensure the attainment of a hydrodynamic steady state (based on the injection of a minimum of 2–3 reactor volumes, (2) the concentration of all elements was constant, within experimental uncertainties. The steady-state concentrations of Ca, Mg (and Si, when possible) were used to calculate R_{Di} following the classical MFR relation linking concentrations and rates:

$$R_{Di,i} = \frac{v \times \Delta[i]}{\eta_i \times SSA \times m_0} \quad (1)$$

where $R_{Di,i}$ (mol.m².s^{-1}) is the dissolution rate of diopside determined with respect to the i^{th} species of diopside, v is the flow rate (l.s^{-1}), $\Delta[i]$ is the difference between the effluent and influent concentrations of a solute i (mol.l^{-1}), η_i is the stoichiometric coefficient of element i

in the mineral, *SSA* is the Kr BET specific surface area ($m^2.g^{-1}$), and m_0 is the initial mass of diopside (g).

2.2 Effect of [SiO_2(aq)] on R_{Di} as a function of surface orientation

The crystallographic orientation of euhedral cm-sized diopside crystals was determined by electron backscatter diffraction (EBSD) using a Zeiss EVO MA10 scanning electron microscope (SEM) (Figs. 1a, b). Because EBSD is a technique sensitive to the first tens of nm of the surface structure, the quality of the diffraction patterns we obtained (e.g. Fig. 1b) ensured that the outermost atomic layers of the diopside surfaces were crystalline prior to the beginning of the experiments. After thorough cleaning in an ethanol ultrasonic bath for ~30 min and rinsing in ultrapure water, selected faces were examined afterwards to determine roughness. Surface roughness at small scales (80 × 80 μm) was measured at a minimum of 5 different areas by atomic force microscopy (AFM) using a Digital Instruments Multimode scanning probe microscope with a Nanoscope IV control system, whereas large scale roughness (1 × 3 mm) was determined with a vertical scanning interferometer (VSI; Wyko NT 3300) in stitching mode. Only the most pristine faces (i.e. pit- and coating-free; mean arithmetic roughness (R_a) ≤ 4 nm for an 80 × 80 μm scan size) were used for running the experiments. When no satisfactory face could be found for a given crystallographic direction, the crystals were cut following calculated angles, polished with a standard protocol using alumina suspensions of decreasing grain sizes and soft polishing cloths; the ultimate step was a final polishing using a colloidal silica suspension. Each crystal was then mounted in a Ti-jig (Fig. 1c). Pressure via a Ti screw was applied to a vitton disk, creating a non-wetted, unreacted reference surface. The jigs were subsequently suspended in a Teflon reactor (120 mL) for a month at 90 °C (Fig. 1d). Average changes in height measured by VSI between the unreacted reference surface and the reacted mineral surface allowed for the determination of the nanoscale dissolution rate of the specific face following:

$$R^{(hkl)} = (\Delta h / t) \times \overline{V}^{-1} \quad (2)$$

where $R^{(hkl)}$ (mol.m^{-2}.s^{-1}) is the dissolution rate of the (*hkl*) face, Δh (m) is the surface retreat, t (s) is time, and $\overline{V}$ (m^3.mol^{-1}) is the molar volume of diopside (Arvidson et al., 2004). In addition, selected areas were scanned weekly *ex situ* by AFM to monitor the evolution of etch pit formation. At pH = 5 the vertical surface retreat was estimated to be too small to be accurately measured by VSI. Consequently, all of the experiments were performed at pH = 1, where the dissolution is much faster (Knauss et al., 1993), either in Si-rich (≥2.2 mM) and Si-poor (≤0.1 mM) solutions. Strictly speaking, comparing the passivating ability of ASSL of experiments conducted at pH = 5 to others at pH = 1 would require that passivation of diopside surface by ASSL is a pH-independent process. Given that the solubility of any SiO_2 polymorph is roughly constant in such a pH range, it was supposed that this was actually the case. Moreover, it is worth mentioning that passivation processes have indeed been reported both in acidic (Daval et al., 2011), circum-neutral (Berger et al., 2002) and slightly alkaline conditions (Daux et al., 1997).

After completion of the surface topography measurements, the samples were carbon coated and thin sections perpendicular to the investigated faces were prepared by focused ion beam (FIB) milling. The thickness and chemical composition of the thin sections were then analyzed by transmission electron microscopy (TEM) at 200 kV (FEI Tecnai G^2). Energy dispersive X-Ray (EDX) line scans were acquired using an EDAX Si–Li detector with ultra-thin window. Energy filtered TEM chemical images and electron energy loss spectra (EELS) were obtained with a postcolumn Gatan GIF imaging filter, using the Ca $L_{2,3}$, O *K*, Mg *K*, and Si *K* edges.

3. Results and Discussion

3.1 Dependence of the bulk dissolution rate of diopside on [SiO_2(aq)]

A typical result from mixed-flow reactor (MFR) experiments is shown in Fig. 2a. After achievement of steady-state conditions, the inlet solution was switched from a Si-rich to a Si-free solution. After a sharp increase, the outlet Ca and Mg concentrations leveled to a plateau ~10 times greater than that observed in the Si-rich solution. Given that steady-state conditions were achieved in both cases, and that neither the mass of the powder nor the flow rate were changed between the two experiments, this directly translates into a dissolution rate ~10 times faster in the Si-free solution compared to the Si-rich condition. The dependence of the diopside dissolution rates on [SiO_2(aq)] was found to be independent of the order in which the experiments were done (i.e. switch from Si-rich to Si-free, or vice versa). Overall, an inverse linear relation was found between the bulk R_{Di} and total [$SiO_{2(aq)}$] (Fig. 2b, see Table 1 for details). Based on the data obtained by Daval et al. (2010), R_{Di} did not depend on the ΔG_r(Di) under our experimental conditions (ΔG_r(Di) ≤ -89 kJ.mol^{-1} for all experiments, see details in section *2.1*), so that it can be confidently concluded that the observed decrease in R_{Di} was a function of [SiO_2(aq)], and not ΔG_r(Di).

These results suggest that diopside crystals are apparently homogeneously covered with a very thin passivating ASSL. Our interpretation is based on the argument that at conditions where amorphous silica is soluble (i.e. where the bulk fluid is undersaturated with respect to amorphous silica), any thin passivating layer that forms is intrinsically unstable, resulting in its subsequent dissolution, which supposedly occurs nearly synchronously with the re-exposure of the pristine diopside surface. The diopside will then dissolve and release Si, which in turn results in a new thin (possibly a few atomic monolayers), passivating (unstable) ASSL forming. This cycle of auto-passivation is consistent with the observation

that (1) the faster the dissolution rate of the passivating silica layer (R_{ASSL}), the faster the concomitant dissolution of diopside (R_{Di}) and (2) because R_{ASSL} depends on the bulk Gibbs free energy for the dissolution of the surface layer (ΔG_r(ASSL)), R_{Di} will depend on [SiO_2(aq)].

The above process can be expressed mathematically in the following manner, where R_{Di} is equivalent to the far-from-equilibrium rate of dissolution of the passivating layer ($R_{-\infty}$), modified by a chemical affinity term ($f(\Delta G_r(\text{ASSL}))$):

$$R_{\text{Di}} \Leftrightarrow R_{\text{ASSL}} = R_{-\infty}.f(\Delta G_r(\text{ASSL})) \quad (3)$$

The chemical affinity term, incorporating ΔG_r(ASSL), can take many forms, depending on the assumed mechanism. Consistent with the linear trend we found (Fig. 2b), we chose to use a simple relation based on transition state theory (Lasaga, 1981):

$$f(\Delta G_r(\text{ASSL})) = 1 - \exp\left(\frac{\Delta G_r(\text{ASSL})}{RT}\right) \quad (4)$$

If one supposes that $a_{\text{SiO2(aq)}}$ is equivalent to [SiO_2(aq)], after re-arrangement, the combination of Eqs. (3) and (4) leads to:

$$R_{\text{Di}} \equiv R_{-\infty} - \frac{R_{-\infty}}{K_s}[\text{SiO}_2(\text{aq})] \quad (5)$$

Thus, in Fig. 2b, the solubility constant of the ASSL (K_s) can be approximated by the intercept of the regression line of $R_{Di} = f$([SiO_2(aq)]) with the x axis, yielding a value of K_s = $10^{-2.66}$. Although our data can be successfully fitted with a rate equation like Eq. (5), whether an equilibrium can be strictly defined for such a system in a bulk thermodynamic sense is subject to question, and further experimental and theoretical research is required to validate such a conceptual framework. Supposing that an equilibrium can be defined, and for the purpose of comparison, the ASSL would be slightly more soluble than α-cristobalite ($K_s^{T=90°C}$(α-cristobalite) = $10^{-2.73}$) and less soluble than pure, anhydrous amorphous silica

($K_s^{T=90°C}$(SiO_2(am) = $10^{-2.23}$), according to the EQ3/6 thermodynamic database. Moreover, the intercept of the regression line of $R_{Di} = f([SiO_2(aq)])$ with the *y* axis yields $R_{Di} = 9.09\times10^{-10}$ mol.m^{-2}.s^{-1}, in excellent agreement with the dissolution rate plateau reported in Daval et al., 2010 ($R_{Di} = 8.76\times10^{-10}$ mol.m^{-2}.s^{-1}). Finally, it can be verified that the data of Daval et al. (2010) obtained at various SiO_2(aq) concentrations (Fig. 2b, white squares) is in reasonable agreement with relation (5). The scatter of the data is likely to be due to the fact that in this previous study, [SiO_2(aq)] was not the only parameter varying from one experiment to the other, because that study's goal was to investigate the effect of stoichiometric saturation state with respect to diopside (ΔG_r(Di)) on R_{Di}. Therefore, in addition to [SiO_2(aq)], other parameters may have affected R_{Di} during the course of some of these previous experiments.

To conclude, the results from the present study suggest that at a macro-scale, the rate-limiting process for diopside dissolution occurs at the outer (bulk fluid/ASSL) interface, due to the impermeable nature of the passivating ASSL that prevents the bulk fluid from reaching the pristine diopside surface. In the following sections, the links between the macro-scale observations and the micro- to nano-scale measurements of diopside dissolution are developed.

3.2 Face-specific dissolution rate of diopside in low-[SiO_2(aq)] solutions

According to Dana (1899), 85 natural forms have been observed for diopside. However, because diopside is an inosilicate (Q^2 structure) with silicate chains parallel to the *c* axis, euhedral crystals are often elongated in this direction, so that the most prevalent faces are those parallel to the *c* axis, in particular: (100); (010); (110) and $(1\bar{1}0)$. To a lesser extent, the faces (001), (111), $(\bar{1}01)$, and more rarely (021), are also encountered. Below we report on the microscopic dissolution features and rates of 6 of these common faces: (100), (010), (110), $(1\bar{1}0)$, (001), and (021).

3.2.1 Surface retreat measurements

The surface retreat measured by VSI for each face is listed in Table 2, and the corresponding dissolution rates (referred to as $R_{\text{low-Si}}^{(hkl)}$) are reported in Table 3. As an example, a typical topographic image of the reacted (001) face is shown in Fig. 3. The non-wetted (masked) surface is revealed by the presence of a raised flat circular area. This reference area contrasts with the adjacent dissolved surface that is thoroughly pitted and has a mean elevation ~5.1 µm lower than the reference level. On the whole, the (*hk*0) faces are much less reactive than the (*hkl*≠0) faces. The face-specific dissolution rates $R_{\text{low-Si}}^{(hkl)}$ observe the following trend: $R_{\text{low-Si}}^{(001)} > R_{\text{low-Si}}^{(021)} >> R_{\text{low-Si}}^{(110)} \approx R_{\text{low-Si}}^{(1\bar{1}0)} \approx R_{\text{low-Si}}^{\text{MFR}} > R_{\text{low-Si}}^{(010)} > R_{\text{low-Si}}^{(100)}$, with $R_{\text{low-Si}}^{\text{MFR}}$ being the extrapolated rate from the results of MFR experiments performed on diopside powders reported in Knauss et al. (1993).

The differences in the face-specific dissolution rates can in part be explained in terms of the crystallographic bonding structure. In the diopside structure, silica tetrahedral units are organized as single chains parallel to the *c*-axis, where each tetrahedron is connected to two others. The dissolution rates will differ for different faces as a function of the number of Si-O-Si bonds that must be broken per tetrahedron. As an example, the retreat of (*hk*0) faces requires the breaking of two Si-O-Si bonds to liberate one Si tetrahedron, whereas the retreat of (001) and (021) faces requires the breaking of only one Si-O-Si bond per Si tetrahedron (Fig. 4). Thus, the dissolution rates of the specific faces fall into two classes: $R^{(001),(021)} >> R^{(hk0)}$. While previously inferred for phyllosilicates (e.g. Turpault and Trotignon, 1994), these results are, to the best of our knowledge, the first direct face-specific measurements that confirm that the connectedness of Si tetrahedrons impacts the dissolution rate of specific crystal faces.

3.2.2 Etch pit formation

The better lateral resolution of AFM compared to that of VSI allowed for a more detailed investigation of the dissolved surface topographies. A common feature of the pits observed on all faces is that their sloping sides merge with pointed bottoms (Fig. EA1 in Electronic Annex), a typical feature of pits arising from dislocation defects in minerals (Dove et al., 2005 and references therein). Whereas the pits formed on (*hk*0) faces are elongated following the *c* axis and relatively small (~ 10 × 3 µm), those formed on the (001) and (021) faces are significantly larger (> 30 × 70 µm) and rounded. The most pitted faces are (110) and $(1\bar{1}0)$, and to a lesser extent, (001). With the notable exception of the (021) face, the pit-volume density ($PVD_{\text{low-Si}}^{(hkl)}$, defined as the volume of pits per diopside unit area) on a given face is correlated with its corresponding dissolution rate (see Fig. EA1 in Electronic Annex; $PVD_{\text{low-Si}}^{(001)} > PVD_{\text{low-Si}}^{(110)} \approx PVD_{\text{low-Si}}^{(1\bar{1}0)} > PVD_{\text{low-Si}}^{(021)} >> PVD_{\text{low-Si}}^{(100)} \geq PVD_{\text{low-Si}}^{(010)}$).

Dislocations in general (e.g. Lasaga and Blum, 1986; Lee and Parsons, 1997), and screw dislocations in particular (e.g. Lasaga and Lüttge, 2001; Dove et al., 2005; Beig and Lüttge, 2006; Arvidson and Lüttge, 2010), have been proposed as a major driving force for mineral dissolution processes. Recently, Amiguet et al. (2010) reported that the most common Burgers vectors for diopside dislocations were by far ½ <110> and [001]. Given that the corresponding screw dislocations outcrop at the surfaces of faces (110) and (001), respectively, this explains why the most pitted faces are faces (110), $(1\bar{1}0)$, and (001). Because faces (110) and $(1\bar{1}0)$ are structurally identical, their reactivities should be identical. This has, in fact, been confirmed in this study, since the values of $R_{\text{low-Si}}^{(hkl)}$, $PVD_{\text{low-Si}}^{(hkl)}$, and $d_{\text{low-Si}}^{(hkl)}$ (thickness of the ASSL, see below) are very similar for these faces. Moreover, faces (110) and $(1\bar{1}0)$ dissolve faster than faces (010) and (100). This result may strengthen the relation between screw dislocations, etch pit density, and rates proposed in previous studies (e.g. Arvidson and Lüttge, 2010). In conclusion, our results support the idea that face-specific

dissolution rates are primarily a function of two parameters, namely silica tetrahedron connectedness and dislocation density. The former parameter appears, however, to be the more important one since $R^{(02\bar{1})}_{\text{low-Si}} >> R^{(110)}_{\text{low-Si}} \approx R^{(1\bar{1}0)}_{\text{low-Si}}$, although $PVD^{(110)}_{\text{low-Si}} \approx PVD^{(1\bar{1}0)}_{\text{low-Si}} > PVD^{(02\bar{1})}_{\text{low-Si}}$.

3.2.3 Surface altered layer formation

Previous investigations of fluid-diopside interfaces have revealed the presence of nm-thick, amorphous Si-rich surface layers (ASSL) (e.g. Petit et al., 1987; Eggleston et al., 1989; Hellmann et al., 2012). Our TEM results show that their thickness ($d^{(hkl)}_{\text{low-Si}}$) is face-dependent. As a first approximation, $d^{(hkl)}_{\text{low-Si}}$ is correlated with the absolute dissolution rate of each face ($d^{(001)}_{\text{low-Si}} \approx d^{(02\bar{1})}_{\text{low-Si}} >> d^{(010)}_{\text{low-Si}} \approx d^{(110)}_{\text{low-Si}} \geq d^{(1\bar{1}0)}_{\text{low-Si}} > d^{(100)}_{\text{low-Si}}$; see Table 3). Interestingly, there could be up to 2 orders of magnitude between the thickest and thinnest layers, which may be an additional explanation why some previous studies failed to find unambiguous evidence for ASSL formation (see discussion in Hellmann et al., 2012).

Energy filtered TEM and TEM-EDX revealed that the ASSL are depleted in Ca and Mg, and composed almost exclusively of SiO_2. For the thickest layers (> 10 nm), the chemical gradients (e.g. Ca) at the inner interface are very sharp, on the order of a few nm (Fig. 5a). Whereas broad cation depletion profiles would have resulted from a mechanism controlled by solid-state volume interdiffusion (Hellmann et al., 2003), indeed, our observations indirectly support the premise that the relatively thicker ASSL (>10 nm) are permeable, allowing unhindered aqueous transport between the pristine mineral surface and the bulk fluid. Consistent with a growing number of studies, the observation that the release of cations is not transport-limited by solid-state diffusion is in better agreement with a mechanism whereby the ASSL formed by interfacial dissolution-precipitation (e.g. Teng et al., 2001; Hellmann et al., 2003; Daval et al., 2009b; Zhang and Lüttge, 2009; King et al., 2011; Hellmann et al., 2012; Ruiz-Agudo et al., 2012). In regard to the much thinner ASSL (<10 nm) formed on (*hk*0)

faces, the measurement of chemical gradients proved to be analytically challenging by TEM, such that we could not make any inferences regarding their transport properties. To address this question, additional experiments were run using solutions with elevated [SiO_2(aq)], followed by VSI measurements of face-specific dissolution rates.

3.3 Face-specific dissolution rates of diopside in elevated [SiO_2(aq)] solutions

Based on the results of the macro-scale experiments, the approximate solubility of the ASSL that presumably passivate diopside is close to $10^{-2.66}$ M. Consequently, the experiments reported below were run with silica-rich input solutions ([SiO_2(aq)] = 2.2 mM). Such conditions stabilized the passivating ASSL (in other words, because the bulk fluid is close to saturation with respect to the ASSL, they should no longer have a tendency to dissolve). The dissolution rates ($R_{\text{hi-Si}}^{(hkl)}$) calculated from the measured surface retreats (Table 2), are reported in Table 3. Quite unexpectedly, the only faces dramatically affected by high silica concentrations were (110) and $(1\bar{1}0)$ (Figs 6a, c and Table 3). However, to make sure that the surface retreats were not underestimated for these two faces, we measured the thicknesses of the ASSL by TEM. Actually, in case the layers are non-passivating (permeable), stabilizing the outer interface results in the subsequent growth of the layers (see e.g. Daval et al., 2009a, b; King et al., 2011), so that the measurement of surface retreat could only result in misleading conclusions (in other words, we can no longer make the approximation that the measured change in height between the reference surface and the ASSL (Δh) is equivalent to the change in height between the reference surface and the reacted diopside surface located beneath the ASSL). We found that $d_{\text{hi-Si}}^{(110)} \approx d_{\text{hi-Si}}^{(1\bar{1}0)} \leq 10\,\text{nm}$ (Fig. EA2 in Electronic Annex), a result which is similar to what we observed in the low-[SiO_2(aq)] experiments. Thus, the striking differences in surface retreats is a real phenomenon. These differences of reactivity were accompanied by changes in surface etch pitting: while deep (~

353 400 nm) triangular pits formed on faces (110) and $(1\bar{1}0)$ in low-[SiO_2(aq)] solutions (Fig. 7a),
354 shallow pits (~ 50 nm) orientated without any obvious crystallographic direction (Fig. 7b)
355 tended to form when the surfaces were reacted in elevated [SiO_2(aq)] solutions. On the other
356 hand, AFM investigations did not reveal any obvious changes in etch pit morphology, depth,
357 and density for the other four faces as function of high and low [SiO_2(aq)].

358 Taken together, these results unexpectedly provide evidence that passivating ASSL
359 uniquely formed on faces (110) and $(1\bar{1}0)$. These results give rise to the following three points
360 of discussion:

361 (1) Why does the macroscopic reactivity of diopside grains seem to be controlled
362 largely by the (110) and $(1\bar{1}0)$ faces?

363 Point number one would suggest that the total surface area of the crushed diopside
364 was mainly comprised of (110) and $(1\bar{1}0)$ planes. In fact, the (110) surface is the dominant
365 cleavage plane of diopside (Dana, 1899). It is thus likely that grains resulting from grinding
366 express mainly (110), $(1\bar{1}0)$, and equivalent planes (Fig. EA3 in Electronic Annex). In
367 addition, the mean $R_{\text{low-Si}}^{\text{MFR}}$ values are about one order of magnitude lower than $R_{\text{low-Si}}^{(001)}$ (see
368 Table 3). This result confirms that the contribution of highly reactive faces such as (001) or
369 (021) to the total surface area of the grains must be minor.

370 (2) Why do we still observe an important surface retreat of faces (010), (001), (021)
371 (and possibly, (100)) when the experiments are initiated in elevated [SiO_2(aq)] solutions,
372 whereas the ASSL are supposedly thermodynamically stable?

373 Indeed, if the ASSL formed on e.g. the (021) faces are both permeable (as suggested
374 in Section *3.2.3*) and stable, the measured surface retreat should be small, and the thickness of
375 the ASSL should be on the order of a few microns. Conversely, stable passivating ASSL
376 should be evidenced by small surface retreats and thin layers (as observed for (110) and $(1\bar{1}0)$

faces). These two scenarios do not correspond to our measurements. Therefore, the observation that the surface retreats did not change between Si-low and Si-rich solutions (at least for (010), (001), (021) faces) ultimately indicates that the ASSL formed on such faces are not stable, so that they keep dissolving. Hence, the solubility of ASSL is not the same for all faces, which indirectly supports the idea that the structure and/or chemistry of ASSL formed on e.g. (001) and (021) diverge from those formed on (110) and $(1\bar{1}0)$ faces.

(3) Perhaps the most fundamental question evoked by this study is: why do passivating ASSL develop only on faces (110) and $(1\bar{1}0)$?

While our study was aimed at deciphering whether the rate-limiting reactions of diopside dissolution occur at (a) the outer (bulk fluid/ASSL) or (b) inner (ASSL/pristine diopside) interface, our results suggest that the answer is neither "(a) nor (b)", but rather "(a) and (b)", as the location of the rate-limiting reactions strongly rely on the bonding structure of diopside. As further developed in Section *3.4*, passivation processes are crucial for extrapolating laboratory-based dissolution rates because the driving force of the reaction is different when a surface is passivated or not (in the former case, the effect of the chemical affinity on steady-state dissolution rate has to be defined with respect to the ASSL, whereas in the latter case, it has to be defined with respect to the silicate).

Interestingly, Figure 4a reveals that the (110) and $(1\bar{1}0)$ faces are the only ones which exclusively intersect Si-O-Mg bonds (or Si-O-Fe, since Fe and Mg share the same crystallographic site). We speculate that this local environment favors the formation of an ASSL which incorporates large amounts of Fe and/or Mg, a specificity which may lead to (or accelerate the rate of formation of) an amorphous silica structure that is passivating. Supporting this argument is the observation that ASSL formed on olivine (an orthosilicate exclusively composed of Si-O-Mg and Si-O-Fe bonds) are passivating as well (Daval et al., 2011), whereas they are not passivating when formed on the (Mg, Fe)-free inosilicate

wollastonite (Daval et al., 2009a, b). The identification of the molecular-scale mechanisms responsible for minor elements modifying the transport properties and/or structure of amorphous silica requires additional research, and based on our current knowledge, any propositions should therefore be considered as speculative. One possible explanation that could account for our observations is that the molar volume of the (Mg, Fe)-bearing ASSL may be greater than that of the parent phase. The positive difference of molar volumes between ASSL and the silicate mineral would lead then to the formation of a protective layer, as generally described, for instance, in Velbel (1993). In any case, although the detailed mechanisms accounting for a specific role for certain cations in modifying the structure and/or molar volume of the ASSL is unclear, we note that their effect on the transport properties of ASSL has been already evidenced in previous studies (e.g. Iler, 1979; Morris and Fletcher, 1987; Cailleteau, et al., 2008). As an example, the incorporation of Zr is thought to be responsible for maintaining an open porous structure in silica layers (Cailleteau, et al., 2008), whereas minor amounts of Fe may favor the formation of impermeable Si-rich phases (Morris and Fletcher, 1987), which would support the results in the present study. On the other hand, King et al. (2011) did not evidence any passivating process during the course of olivine silicification experiments, which would seem to contradict the above-mentioned mechanism. While this observation points out that a detailed understanding of passivation processes deserves more work, one possible explanation could be that their experiments were conducted in high ionic strength media ($> 2M$), resulting in the presumable complexation of Fe and Mg in the solution, such that less Fe and Mg were available for modifying the ASSL structure.

3.4 Why does passivation matter? Bridging the gap between field and laboratory rates

Beyond being an important issue in the field of materials sciences and geochemistry, characterizing fluid/solid interfaces and understanding which part of the interfacial zone

(inner vs. outer interface) plays the major role in the rate-limiting process during dissolution of silicate minerals has major implications for our ability to correctly use laboratory data to model the rates of chemical weathering reactions in the field. In the vast majority of past and present experimental studies, silicate dissolution rates ($R_{silicate}$) are determined under so-called "far-from-equilibrium" conditions, where dissolved silica concentrations are low, and therefore do not influence $R_{silicate}$. Moreover, all of the geochemical codes that we are aware of do not integrate the presence of ASSL, which potentially should be treated as individual, separate phases, whose solubility may control the dissolution rate of the underlying silicate minerals. In general, geochemical codes treat the chemical saturation of the bulk fluid in terms of the following formalism:

$$R_{\text{silicate}} = R_{-\infty} . f(\Delta G_r(\text{silicate})) \tag{6}$$

where:

$$f(\Delta G_r(\text{silicate})) = 1 - \exp\left(\frac{\Delta G_r(\text{silicate})}{RT}\right) \tag{7}$$

In Eq. (6), the measured far-from-equilibrium rates ($R_{-¥}$) are adjusted to conditions closer-to-equilibrium with the chemical affinity function given by (7), which is a function of the Gibbs free energy for silicate mineral dissolution reaction (ΔG_r(silicate)). Conceptually, this relation implies that ASSL do not exist, or that they are so porous that their presence does not matter, such that the rate-limiting step(s) occur(s) at the silicate/water interface. Very importantly, the present study demonstrates that this assumption is not always correct, and that for specific cases (discussed below), rate laws in the form of Eq. (3) should be considered for more accurately modeling the effect of fluid composition on silicate dissolution rates, as has already been proposed for silicate glasses (Grambow and Muller, 2001). Failure to account for the effects of passivating ASSL may result in a significant overestimation of dissolution rates. Given that laboratory dissolution rates generally are orders of magnitude

451 higher than their natural counterparts (White et al., 1996; White and Brantley, 2003; Maher et
452 al., 2004), it is worth assessing whether or not passivation is an (additional) likely mechanism
453 for bridging the gap between laboratory and field rates. The geological relevance of this
454 proposition will rely on both (1) rock and (2) fluid compositions encountered in the field:

455 (1) Based on the results in the present study, we suggest that chemical weathering
456 reactions of rocks that contain large amounts of (Mg, Fe)-rich silicates, such as (ultra)basic
457 rocks and basalts, are potentially affected by passivation. Interestingly, it is estimated that up
458 35% of the CO_2 consumed by continental silicate alteration is attributed to basalts, making
459 these rocks important actors of chemical weathering (Dessert al., 2003) and the C cycle.
460 Knowledge that a strong coupling exists between physical and chemical erosion (Gaillardet et
461 al., 1999), it is likely that in active weathering terrains, minerals are primarily broken up
462 following dominant cleavage directions. Thus, the reactivity of pyroxenes in the field
463 probably mimics that of the diopside grains investigated in this study (Fig. 2b), similar to the
464 cases of olivine (Daval et al., 2011) and basaltic glass (Daux et al., 1997).

465 (2) With respect to aqueous fluids, one could consider the chemical composition of
466 rivers as a potential, "average" integrated model for the various environments encountered in
467 the field. The chemical compositions of rivers draining either basaltic environments (where
468 pyroxenes are common rock-forming minerals) or other continental environments are taken
469 into account below. Considering [SiO_2(aq)] in rivers as a proxy for chemical weathering and
470 CO_2 consumption (Gaillardet et al., 1999), an interesting observation is that SiO_2(aq) ranges
471 over a wide range of concentrations, from a few tens of µM to several hundreds of µM
472 (Gaillardet, et al., 1999; Louvat and Allègre, 1997, 1998; Louvat et al., 2008). Considering a
473 simple estimation, one can use the chemical composition of rivers to calculate the
474 corresponding ΔG_r values with respect to diopside and to a passivating ASSL, assuming that
475 its solubility is close to that of cristobalite (see Section *3.1*). Obviously, such a value may

vary with the chemical composition of the ASSL (see discussion in Section *3.3*), but from the results of the present study, ASSL with solubility close cristobalite are passivating, whereas ASSL with higher solubility (e.g. those formed on (001) and (021) faces) are permeable. It is noteworthy that aside from a few exceptions, all of the reported rivers are largely undersaturated with respect to diopside, whereas they are rather close to saturation with respect to cristobalite (Fig. 8a). The effect of such ΔG_r values on the dissolution rates of silicates like diopside, following either relation (4) or (7), is represented in Fig. 8b. For most of the considered rivers, the chemical conditions are such that using relation (7) instead of (4) would result in an overestimation of dissolution rates by one or more orders of magnitude. For one third of the reported rivers, the waters are even slightly oversaturated with respect to cristobalite, implying conditions of stability (i.e. dissolution rates ~ 0) for any passivating ASSL present on diopside, or other mafic minerals and/or glasses.

Such simple calculations illustrate how passivation matters in the context of chemical weathering. Passivation is also important for current topics like CO_2 sequestration and related carbonation processes of mafic silicates. As an example, at conditions relevant to CO_2 sequestration (e.g. $T \leq 90°C$), it can be easily calculated that in closed systems, the dissolution of minerals typical of basalts (e.g. olivine, pyroxenes) results in the attainment of saturation with respect to SiO_2 polymorphs, even including highly soluble pure amorphous silica, prior to that of (Ca, Mg) carbonates. The formation of passivating ASSL would result in a difference of several orders of magnitude between the predicted and measured extents of carbonation, as has been experimentally shown for olivine recently (Daval et al., 2011). Such unexpected effects must be taken into account to better assess whether mineral carbonation is a viable process for sequestering anthropogenic CO_2.

4. Conclusions

By investigating diopside dissolution from the nano- to the macro-scale, our study provides new insights on how bulk silicate reactivity is related to complex face-specific behavior at the nanoscale. In conjunction with knowledge of the diopside crystal structure, certain key parameters dictating the transport properties of surface layers were presumably identified, thereby linking our nano- and macro-scale measurements. In particular, we show how nm-thick Si-rich layers (ASSL) sandwiched in between the bulk fluid and the pristine mineral surface may ultimately control silicate reactivity. This has important consequences because it provides additional directions for bridging the gap between laboratory and field measurements. This study has also demonstrated that deriving dissolution mechanisms and rate laws from bulk, macroscopic experiments without a detailed knowledge of the interfacial processes is not without risks. Instead, the deciphering of the interplay of nano- and macro-scale phenomena is likely to represent the future direction of experimental fluid-mineral interaction studies. In addition, the next step forward should be to investigate the transport properties of ASSL formed on feldspars, which represent by far the most abundant group of minerals in the continental crust. Interestingly, the few published studies that indirectly addressed the question as to whether or not ASSL formed on feldspars are porous and permeable enough for not impeding fluid access to the pristine surface of the underlying crystal led to opposite conclusions (e.g. compare the conclusions of Jordan et al. (1999) on anorthite and Hellmann et al. (2003) on labradorite to those obtained by Berger al. (2002) on sanidine). Supposing that ASSL are commonplace in natural geological systems (e.g. Zhu et al., 2006; Hellmann et al., 2012), the abovementioned discrepancies emphasize the need for further detailed studies on the transport properties of ASSL formed on feldspar surfaces under diverse physical and chemical conditions.

Acknowledgements

J.P. Icenhower (LBNL), A. Fernandez-Martinez (LBNL, presently at ISTerre) and K. Benzerara (IMPMC) are warmly acknowledged for their constructive comments throughout this study. The technical help of T. Teague (UC Berkeley), T. Critelli (Univ. Calabria), and A. Schreiber (GFZ) was much appreciated. This work was supported by the Director, Office of Science, Office of Basic Energy Sciences, Chemical Sciences, Geosciences, and Biosciences Division, of the U.S. Department of Energy under Contract No. DE-AC02-05CH11231. The careful reviews and supportive comments by Dr. R.S. Arvidson, as well as two anonymous reviewers, were much appreciated and helped improve the manuscript.

References

Amiguet, E., Cordier, P., and Raterron, P., 2010. Deformation of diopside single crystals at mantle pressure. TEM characterization of dislocation microstructures. *European Journal of Mineralogy* **22**, 181-187.

Arvidson, R. S., Beig, M. S., and Luttge, A., 2004. Single-crystal plagioclase feldspar dissolution rates measured by vertical scanning interferometry. *Am Mineral* **89**, 51-56.

Arvidson, R. S. and Luttge, A., 2010. Mineral dissolution kinetics as a function of distance from equilibrium - New experimental results. *Chem Geol* **269**, 79-88.

Beaulieu, E., Godderis, Y., Donnadieu, Y., Labat, D., and Roelandt, C., 2012. High sensitivity of the continental-weathering carbon dioxide sink to future climate change. *Nat Clim Change* **2**, 346-349.

Beig, M. S. and Luttge, A., 2006. Albite dissolution kinetics as a function of distance from equilibrium: Implications for natural feldspar weathering. *Geochim Cosmochim Ac* **70**, 1402-1420.

546 Berger, G., Beaufort, D., and Lacharpagne, J. C., 2002. Experimental dissolution of sanidine
547 under hydrothermal conditions: Mechanism and rate. *American Journal of Science*
548 **302**, 663-685.
549 Cailleteau, C., Angeli, F., Devreux, F., Gin, S., Jestin, J., Jollivet, P., and Spalla, O., 2008.
550 Insight into silicate-glass corrosion mechanisms. *Nature Materials* **7**, 978-983.
551 Dana, E. S., 1899. *The system of mineralogy*, New York.
552 Daux, V., Guy, C., Advocat, T., Crovisier, J. L., and Stille, P., 1997. Kinetic aspects of
553 basaltic glass dissolution at 90 degrees C: role of aqueous silicon and aluminium.
554 *Chem Geol* **142**, 109-126.
555 Daval, D., Hellmann, R., Corvisier, J., Tisserand, D., Martinez, I., and Guyot, F., 2010.
556 Dissolution kinetics of diopside as a function of solution saturation state: Macroscopic
557 measurements and implications for modeling of geological storage of CO2. *Geochim*
558 *Cosmochim Ac* **74**, 2615-2633.
559 Daval, D., Martinez, I., Corvisier, J., Findling, N., Goffe, B., and Guyot, F., 2009a.
560 Carbonation of Ca-bearing silicates, the case of wollastonite: Experimental
561 investigations and kinetic modeling. *Chem Geol* **265**, 63-78.
562 Daval, D., Martinez, I., Guigner, J. M., Hellmann, R., Corvisier, J., Findling, N., Dominici,
563 C., Goffe, B., and Guyot, F., 2009b. Mechanism of wollastonite carbonation deduced
564 from micro- to nanometer length scale observations. *Am Mineral* **94**, 1707-1726.
565 Daval, D., Sissmann, O., Menguy, N., Saldi, G. D., Guyot, F., Martinez, I., Corvisier, J.,
566 Garcia, B., Machouk, I., Knauss, K. G., and Hellmann, R., 2011. Influence of
567 amorphous silica layer formation on the dissolution rate of olivine at 90 degrees C and
568 elevated pCO(2). *Chem Geol* **284**, 193-209.

569 Dessert, C., Dupré, B., Gaillardet, J., François, L. M., and Allègre, C. J., 2003. Basalt
570 weathering laws and the impact of basalt weathering on the global carbon cycle. *Chem*
571 *Geol* **202**, 257-273.
572 Dove, P. M., Han, N. Z., and De Yoreo, J. J., 2005. Mechanisms of classical crystal growth
573 theory explain quartz and silicate dissolution behavior. *Proceedings of the National*
574 *Academy of Sciences of the United States of America* **102**, 15357-15362.
575 Eggleston, C. M., Hochella, M. F., and Parks, G. A., 1989. Sample Preparation and Aging
576 Effects on the Dissolution Rate and Surface-Composition of Diopside. *Geochim*
577 *Cosmochim Ac* **53**, 797-804.
578 Fritz, B., Jacquot, E., Jacquemont, B., Baldeyrou-Bailly, A., Rosener, M., and Vidal, O.,
579 2010. Geochemical modelling of fluid-rock interactions in the context of the Soultz-
580 sous-Forets geothermal system. *Cr Geosci* **342**, 653-667.
581 Frugier, P., Gin, S., Minet, Y., Chave, T., Bonin, B., Godon, N., Lartigue, J. E., Jollivet, P.,
582 Ayral, A., De Windt, L., and Santarini, G., 2008. SON68 nuclear glass dissolution
583 kinetics: Current state of knowledge and basis of the new GRAAL model. *Journal of*
584 *Nuclear Materials* **380**, 8-21.
585 Gaillardet, J., Dupré, B., Louvat, P., and Allègre, C. J., 1999. Global silicate weathering and
586 CO2 consumption rates deduced from the chemistry of large rivers. *Chem Geol* **159**,
587 3-30.
588 Geisler, T., Janssen, A., Scheiter, D., Stephan, T., Berndt, J., and Putnis, A., 2010. Aqueous
589 corrosion of borosilicate glass under acidic conditions: A new corrosion mechanism.
590 *Journal of Non-Crystalline Solids* **356**, 1458-1465.
591 Godderis, Y., Williams, J. Z., Schott, J., Pollard, D., and Brantley, S. L., 2010. Time
592 evolution of the mineralogical composition of Mississippi Valley loess over the last 10
593 kyr: Climate and geochemical modeling. *Geochim Cosmochim Ac* **74**, 6357-6374.

Grambow, B. and Muller, R., 2001. First-order dissolution rate law and the role of surface layers in glass performance assessment. *Journal of Nuclear Materials* **298**, 112-124.

Hellmann, R., Penisson, J.-M., Hervig, R. L., Thomassin, J.-H., and Abrioux, M.-F., 2003. An EFTEM/HRTEM high-resolution study of the near surface of labradorite feldspar altered at acid pH: evidence for interfacial dissolution-reprecipitation. *Physics and Chemistry of Minerals* **30**, 192-197.

Hellmann, R., Wirth, R., Daval, D., Barnes, J.-P., Penisson, J.-M., Tisserand, D., Epicier, T., Florin, B., and Hervig, R. L., 2012. Unifying natural and laboratory chemical weathering with interfacial dissolution–reprecipitation: A study based on the nanometer-scale chemistry of fluid–silicate interfaces. *Chem Geol* **294–295**, 203-216.

Iler, R.K., 1979. The Chemistry of Silica. John Wiley & Sons, New York.

Jordan, G., Higgins, S. R., Eggleston, C. M., Swapp, S. M., Janney, D. E., and Knauss, K. G., 1999. Acidic dissolution of plagioclase: In-situ observations by hydrothermal atomic force microscopy. *Geochim Cosmochim Ac* **63**, 3183-3191.

King, H. E., Plumper, O., Geisler, T., and Putnis, A., 2011. Experimental investigations into the silicification of olivine: Implications for the reaction mechanism and acid neutralization. *Am Mineral* **96**, 1503-1511.

Knauss, K. G., Johnson, J. W., and Steefel, C. I., 2005. Evaluation of the impact of CO2, co-contaminant gas, aqueous fluid and reservoir rock interactions on the geologic sequestration of CO2. *Chem Geol* **217**, 339-350.

Knauss, K. G., Nguyen, S. N., and Weed, H. C., 1993. Diopside dissolution kinetics as a function of pH, CO2, temperature, and time. *Geochim Cosmochim Ac* **57**, 285-294.

Lasaga, A. C., 1981. Transition State Theory. In: Lasaga, A. C., and Kirkpatrick, R.J (Ed.), *Kinetics of Geochemical Process*. Mineralogical Society of America.

Lasaga, A. C. and Blum, A. E., 1986. Surface chemistry, etch pits and mineral-water reactions. *Geochim Cosmochim Ac* **50**, 2363-2379.

Lasaga, A. C. and Luttge, A., 2001. Variation of Crystal Dissolution Rate Based on a Dissolution Stepwave Model. *Science* **291**, 2400-2404.

Le Hir, G., Ramstein, G., Donnadieu, Y., and Godderis, Y., 2008. Scenario for the evolution of atmospheric pCO(2) during a snowball Earth. *Geology* **36**, 47-50.

Lee, M. R., Hodson, M. E., Brown, D. J., MacKenzie, M., and Smith, C. L., 2008. The composition and crystallinity of the near-surface regions of weathered alkali feldspars. *Geochim Cosmochim Ac* **72**, 4962-4975.

Lee, M. R. and Parsons, I., 1997. Dislocation formation and albitization in alkali feldspars from the Shap granite. *Am Mineral* **82**, 557-570.

Louvat, P. and Allegre, C. J., 1997. Present denudation rates on the island of Reunion determined by river geochemistry: Basalt weathering and mass budget between chemical and mechanical erosions. *Geochim Cosmochim Ac* **61**, 3645-3669.

Louvat, P. and Allegre, C. J., 1998. Riverine erosion rates on Sao Miguel volcanic island, Azores archipelago. *Chem Geol* **148**, 177-200.

Louvat, P., Gislason, S. R., and Allegre, C. J., 2008. Chemical and mechanical erosion rates in Iceland as deduced from river dissolved and solid material. *American Journal of Science* **308**, 679-726.

Luce, R. W., Bartlett, R. W., and Parks, G. A., 1972. Dissolution kinetics of magnesium silicates. *Geochim Cosmochim Ac* **36**, 33-50.

Maher, K., 2010. The dependence of chemical weathering rates on fluid residence time. *Earth Planet Sc Lett* **294**, 101-110.

Maher, K., DePaolo, D. J., and Lin, J. C. F., 2004. Rates of silicate dissolution in deep-sea sediment: In situ measurement using U-234/U-238 of pore fluids. *Geochim Cosmochim Ac* **68**, 4629-4648.

Maher, K., Steefel, C. I., White, A. F., and Stonestrom, D. A., 2009. The role of reaction affinity and secondary minerals in regulating chemical weathering rates at the Santa Cruz Soil Chronosequence, California. *Geochim Cosmochim Ac* **73**, 2804-2831.

Morris, R. C. and Fletcher, A. B., 1987. Increased solubility of quartz following ferrous ferric iron reactions. *Nature* **330**, 558-561.

Nugent, M. A., Brantley, S. L., Pantano, C. G., and Maurice, P. A., 1998. The influence of natural mineral coatings on feldspar weathering. *Nature* **395**, 588-591.

Petit, J. C., Dellamea, G., Dran, J. C., Schott, J., and Berner, R. A., 1987. Mechanism of diopside dissolution from hydrogen depth profiling. *Nature* **325**, 705-707.

Ruiz-Agudo, E., Putnis, C. V., Rodriguez-Navarro, C., and Putnis, A., 2012. Mechanism of leached layer formation during chemical weathering of silicate minerals. *Geology* **40**, 947-950.

Teng, H. H., Fenter, P., Cheng, L. W., and Sturchio, N. C., 2001. Resolving orthoclase dissolution processes with atomic force microscopy and X-ray reflectivity. *Geochim Cosmochim Ac* **65**, 3459-3474.

Turpault, M. P. and Trotignon, L., 1994. The Dissolution of Biotite Single-Crystals in Dilute Hno3 at 24-Degrees-C - Evidence of an Anisotropic Corrosion Process of Micas in Acidic Solutions. *Geochim Cosmochim Ac* **58**, 2761-2775.

van der Lee, J. and De Windt, L., 2002. *CHESS Tutorial and Cookbook. Updated for version 3.0.*, Paris.

Velbel, M. A., 1993. Formation of protective surface layers during silicate-mineral weathering under well-leached, oxidizing conditions. *Am Mineral* **78**, 405-414

White, A. F., Blum, A. E., Schulz, M. S., Bullen, T. D., Harden, J. W., and Peterson, M. L., 1996. Chemical weathering rates of a soil chronosequence on granitic alluvium .1. Quantification of mineralogical and surface area changes and calculation of primary silicate reaction rates. *Geochim Cosmochim Ac* **60**, 2533-2550.

White, A. F. and Brantley, S. L., 2003. The effect of time on the weathering of silicate minerals: why do weathering rates differ in the laboratory and field? *Chem Geol* **202**, 479-506.

Zhang, L. and Luettge, A., 2009. Theoretical approach to evaluating plagioclase dissolution mechanisms. *Geochim Cosmochim Ac* **73**, 2832-2849.

Zhu, C., 2005. In situ feldspar dissolution rates in an aquifer. *Geochim Cosmochim Ac* **69**, 1435-1453.

Zhu, C., Veblen, D. R., Blum, A. E., and Chipera, S. J., 2006. Naturally weathered feldspar surfaces in the Navajo Sandstone aquifer, Black Mesa, Arizona: Electron microscopic characterization. *Geochim Cosmochim Ac* **70**, 4600-4616.

Figure legends

Fig. 1. Face-specific diopside dissolution experiments. (a) The first steps consisted in identifying the crystallographic orientation of selected diopside faces by EBSD based on (b) the indexation of diffraction patterns. (c) After initial surface roughness measurements by AFM and VSI (necessitating potential re-polishing of the samples), the crystals were mounted on a Ti-jig. Pressure via a Ti screw was applied to a vitton disk (effective diameter: 1.44 mm), creating a non-wetted reference surface. (d) The jig was suspended in a Teflon reactor for a month.

Fig. 2. Diopside dissolution rate measured in a MFR using 300-500 µm grain-sized powders. (a) Measured concentrations of Ca (circles) and Mg (triangles) released as a function of time.

After 18 days, the inlet solution was changed, from [SiO_2(aq)] = 2.09 mM to [SiO_2(aq)] = 38 µM, all other parameters being kept constant. This resulted in a substantial increase of Ca and Mg release. (b) Steady-state diopside dissolution rates (blue diamonds) plotted as a function of total [SiO_2(aq)], showing an inverse linear relation. For comparison, the data of Daval et al. (2010) are reported as well (white squares). Note that only their data for which $\Delta[i] > 0$ (and thus $R_{Di} > 0$) are reported, and that this dataset was not used for computing the linear regression depicted in this figure –see text for additional details.

Fig. 3. 3D-view of face (001) reacted at 90°C and pH = 1 for one month in a silica-free solution. The reference area, where the mask was during the experiment, is 5.1 µm above the level of the dissolved surface, which appears to be heavily pitted. 3D-view realized by stitching VSI images on an area of 1.9 × 1.3 mm.

Fig. 4. Projections of diopside structure following (a) [001] and (b) [100] zone axes. The silicate tetrahedrons are blue; calcium, magnesium and oxygen atoms are white, green, and red spheres, respectively. Among the investigated faces, (001) and (021) are the only planes that intersect only one Si-O-Si bond per silicate tetrahedron. Conversely, dissolution normal to (*hk*0) faces will intersect two Si-O-Si bonds per tetrahedron. Cleavage planes (110) and $(1\bar{1}0)$ intersect Si-O-Mg (or Si-O-Fe) bonds only.

Fig. 5. TEM images of fluid/diopside interfaces realized on FIB thin sections perpendicular to (a) (021) and (b) (110) faces after chemical weathering in Si-free solutions. For both cases, an amorphous Si-rich surface layer (ASSL) is evidenced, with thicknesses of ~103 nm for the (021) face and ~4–9 nm for the (110) face (red arrows). For both FIB thin sections, a ~100-nm thick carbon (C) coating and a platinum layer were deposited to protect the underlying

surfaces during ion beam milling. The insert in Fig. 5a shows a typical EFTEM calcium profile across ASSL formed on the (021) face. It reveals a sharp nm-scale chemical concentration jump between the Ca-depleted ASSL and the pristine diopside. Note that an HRTEM image of the diopside/ASSL contact is provided in the Electronic Annex (Fig. EA4).

Fig. 6. VSI-measured surface dissolution of 4 different crystal reacted for one month in (a, b) Si-free and (c, d) Si-rich solutions, exposing faces (a, c) (110) and (b, d) (001). The reference (masked) surface is located at $z \sim 0$. In Si-free solutions, the (*hk*0) faces were much less reactive than the (001) and (021) faces (i.e. compare retreat of (a) face (110) with (b) (001)). Note that the (001) face was hardly affected by high concentrations of SiO_2(aq), whereas the dissolution of (110) decreased by ~1 order of magnitude. For comparison, far-from-equilibrium bulk dissolution rates from powders (Knauss et al., 1993) would be equivalent to a mean retreat of $\Delta h_{\text{low-Si}} = 614$ nm.

Fig. 7. Representative AFM images of two different crystals rinsed beforehand in ultrapure water, and exposing faces $(1\bar{1}0)$ after 15 days of alteration in (a) Si-free and (b) Si-rich solutions. The plots on the right hand side of the figures represent topographic profiles from left to right along the corresponding white lines. Well-defined, deep triangular pits formed on the surface of the $(1\bar{1}0)$ face of diopside in the Si-free solution; pitting was more irregular in the Si-rich solution, with depths < 50 nm. Note that the measured thickness of the ASSL formed on the faces $(1\bar{1}0)$ during the course of each experiment never exceeded 10 nm (see text and Table 3), such that their formation does not prevent observation of etch pit formation on these faces.

Fig. 8. Plots showing the potential importance of passivation phenomena in terms of bridging the gap between laboratory and field weathering rates. The chemical compositions of rivers draining either basaltic environments (Iceland (triangles), Azores (squares), and Réunion (circles)) or other continental silicates (diamonds) were used to calculate the Gibbs free energy of diopside (ΔG_r(Di)) and cristobalite (ΔG_r(Crs)) dissolutions, using CHESS. Figure 8a shows that almost all rivers are very undersaturated with respect to diopside (ΔG_r(Di) << 0), whereas they are close to saturation or even supersaturated with respect to cristobalite (Crs), whose solubility was taken as a possible analog for that of ASSL formed on faces (110) and $(1\bar{1}0)$ of diopside. (b) Consequences of this from a kinetic standpoint. The effect of fluid composition is translated through the values of the $f(\Delta G_r)$ functions, considering either ΔG_r(Di) (x axis) (Eq. 7) or ΔG_r(Crs) (y axis) (Eq. 4). The dashed line represents a 1:1 relation between $f(\Delta G_r$(Di)) and $f(\Delta G_r$(Crs)). Nearly all data points fall below this line, in particular for basaltic environments. Therefore, implementing the $f(\Delta G_r$(Crs)) function into geochemical codes, in agreement with passivation process, has the potential to lower the laboratory-based rates by several orders of magnitude. The insert in Fig. 8b is a close-up of the area circled in blue. Chemical compositions of the main rivers taken from Louvat and Allègre (1997) for Réunion, Louvat and Allègre (1998) for Azores, Louvat et al. (2008) for Iceland, and Gaillardet et al. (1999) for other environments, considering only the rivers for which silicates contribute more than 20% of the total dissolved load in the river (see Gaillardet et al. (1999) for details).

Table 1. Summary of experimental and calculated data concerning the dissolution of diopside in MFR.

Expt.	time	m_0	v	$[Si]_{in}$	$[Ca]_{out}$	$[Mg]_{out}$	$[Si]_{out}$	$pH^{in}_{(20°C)}$	$pH^{out}_{(20°C)}$	$pH_{in\ situ}{}^{a}$	$pH_{in\ situ}{}^{b}$	r_{Ca}	r_{Mg}	r_{Si}	r_{Avg}	$\Delta G_r{}^{a}$	$\Delta G_r{}^{b}$	r_{Avg}(pH = 5)
DPS-M	16	0.3212	1.6E-06	6.33	5.52	5.40	16.3	4.84	4.84	4.98	4.98	9.72E-10	1.00E-09	8.97E-10	9.57E-10	-117.9	-117.9	9.49E-10
DPS-O	21	0.6627	6.7E-07	121	21.6	18.5	160	4.82	4.86	4.98	5.01	7.68E-10	6.92E-10	7.11E-10	7.24E-10	-96.4	-95.6	7.24E-10
DPS-P	20	0.2859	6.3E-07	17.8	11.8	11.1	37.2	4.83	4.85	4.97	5.00	9.15E-10	9.05E-10	7.71E-10	8.64E-10	-108.6	-108.0	8.60E-10
DPS-Q	16	0.4393	6.7E-07	115	15.5	14.7	147	4.82	4.86	4.98	5.00	8.32E-10	8.30E-10	8.80E-10	8.47E-10	-98.7	-97.9	8.44E-10
DPS-R	14	0.2859	6.7E-07	768	6.8	6.3	776	4.83	4.82	4.98	4.96	5.61E-10	5.47E-10	3.38E-10	5.54E-10	-93.7	-94.1	5.47E-10
DPS-S	18	0.4938	6.3E-07	1473	6.6	6.1	1480	4.83	4.85	4.98	4.99	3.00E-10	2.90E-10	1.63E-10	2.95E-10	-90.2	-89.8	2.93E-10
DPS-T	15	0.4938	5.8E-07	121	19.9	19.7	164	4.82	4.82	4.98	4.96	8.31E-10	8.66E-10	9.14E-10	8.71E-10	-96.3	-96.7	8.60E-10
DPS-U	14	0.4924	5.8E-07	436	18.4	18.3	473	4.79	4.79	4.95	4.94	7.71E-10	8.07E-10	7.95E-10	7.91E-10	-91.3	-91.5	7.74E-10
DPS-V	19	0.4981	6.3E-07	2090	1.43	1.45	2024	4.84	4.85	4.98	4.99	6.43E-11	6.86E-11	-1.52E-09	6.64E-11	-97.2	-96.9	6.62E-11
DPS-W	14	0.4981	8.7E-07	7.00	15.2	15.3	38.4	4.76	4.81	4.91	4.96	9.35E-10	9.90E-10	9.90E-10	9.72E-10	-108.3	-107.2	9.48E-10

Columns 1-4 indicate: name of the experiment, total duration time (days), initial mass of diopside (grams), flow rate of the pump ($L.s^{-1}$). The input ($[Si]_{in}$) and output ($[Ca]_{out}$, $[Mg]_{out}$ and $[Si]_{out}$) solution compositions are indicated in the next four columns (µM) (at the beginning of the experiment, $[Ca]_{in} = [Mg]_{in} = 0$). The pH of the input and output solutions measured at room temperature are reported in the columns labelled $pH^{in}_{(20°C)}$ and $pH^{out}_{(20°C)}$. These values were used to calculate the *in situ* pH based either (a) on the initial pH and the effluent concentration of species or ($pH_{in\ situ}{}^{a}$) (b) on the outlet pH measured at 20°C ($pH_{in\ situ}{}^{b}$). The dissolution rates based on each major constituting element of diopside, as well as the unweighted average of the dissolution rate are reported in the subsequent column ($mol.m^2.s^{-1}$) (note: this average rate does not include the values of r_{Si} if $\left|1-[Si]_{in}/[Si]_{out}\right| \le 0.05$, which is the analytical limit). The two ΔG columns indicate ΔG_r values ($kJ.mol^{-1}$) with respect to diopside dissolution at which the steady-state dissolution rates were measured, based either on $pH_{in\ situ}{}^{a}$ or on $pH_{in\ situ}{}^{b}$. The final column corresponds to r_{Avg} recalculated for an exact pH of 5.00, adjusted from r_{Avg} , based on the pH-dependence of diopside dissolution given in Knauss et al., 1993. Note that the experiments DPS-R, DPS-T and DPS-W represent the continuation of experiments DPS-P, DPS-S, and DPS-V respectively. The only parameter that was changed between these couples of experiments was the composition of the inlet solution (column 4).

Table 2. Summary of the surface retreat measurements performed on 12 different crystals.

Face	$\Delta h_{\text{low-Si}}$ [nm]	t [d]	$\Delta h_{\text{hi-Si}}$ [nm]	t [d]
(100)	160	30.21	96	30.50
(010)	416	30.62	373	29.30
(001)	5070	27.83	4593	27.55
(110)	624	29.70	45	32.14
$(1\bar{1}0)$	464	27.97	60	30.16
(021)	3625	27.97	3973	31.02

The orientation of the face analyzed for each crystal is indicated in column 1. The results of experiments performed in Si-free solutions are listed in columns 2 and 3, those from experiments performed in Si-rich solutions in columns 4 and 5. The differences in elevation (= surface retreat) between the masked and unmasked areas ($\Delta h_{\text{low-Si}}$ and $\Delta h_{\text{hi-Si}}$) are reported in columns 2 and 4, with the corresponding time durations of the experiments in columns 3 and 5, respectively.

Table 3. Summary of the face-specific dissolution rates of diopside and measurement of the thickness of ASSL formed in Si-free solution.

Face	$R_{\text{low-Si}}^{(hkl)}$ [mol/m²/s]	$R_{\text{hi-Si}}^{(hkl)}$ [mol/m²/s]	$\frac{R_{\text{hi-Si}}^{(hkl)}}{R_{\text{low-Si}}^{(hkl)}}$	$\frac{R_{\text{low-Si}}^{(hkl)}}{R_{\text{low-Si}}^{\text{MFR}}}$	$d_{\text{low-Si}}^{(hkl)}$ [nm]
(100)	9.30E-10	5.53E-10	0.59*	0.26	≤ 1
(010)	2.39E-09	2.24E-09	0.94	0.66	9-15
(001)	3.20E-08	2.93E-08	0.92	8.90	98
(110)	3.69E-09	2.46E-10	0.07	1.03	4-9
$(1\bar{1}0)$	2.91E-09	3.49E-10	0.12	0.81	1-5
(021)	2.28E-08	2.25E-08	0.99	6.33	103

The orientation of the face analyzed for each of the 12 crystals is indicated in column 1. The dissolution rates for each face, either in Si-free (column 2) or in Si-rich (column 3) solution, were calculated following Eq. (2). Column 4 represents the normalization of the face-specific rates obtained in Si-rich solutions to those obtained far from equilibrium, in Si-free solutions. Column 5 is the normalization of the far-from-equilibrium face-specific dissolution rates to that of a diopside powder (extrapolated from far-from-equilibrium MFR experiments reported in Knauss et al., 1993). Column 6 is the thickness of the ASSL formed on each face for the experiments run in Si-free solutions.

*Given that corresponding measured profiles reported in Table 2 vary by ± 30 nm, the question as to whether or not the face (100) is affected by high aqueous silica concentrations remains an open question.

Figure 1

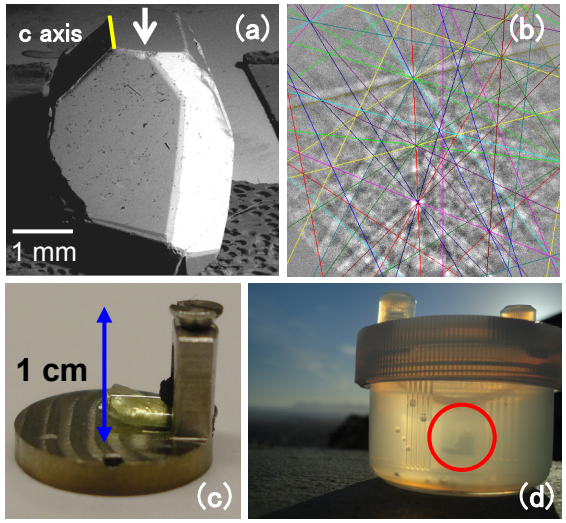

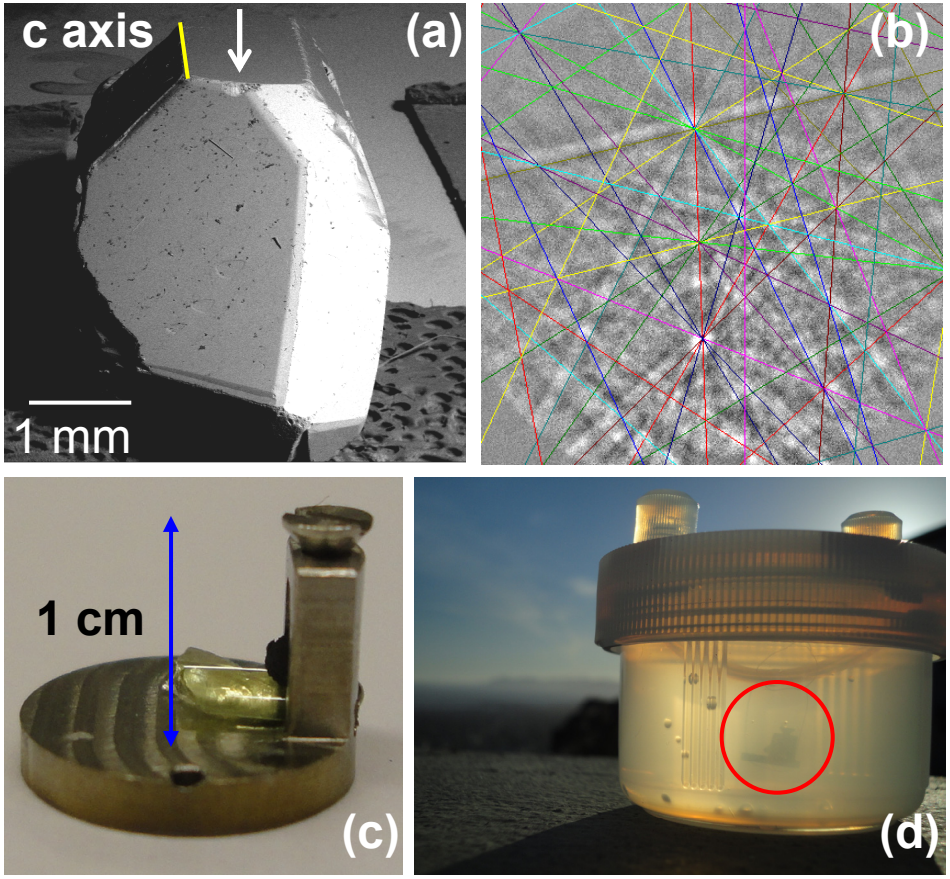

Figure 2

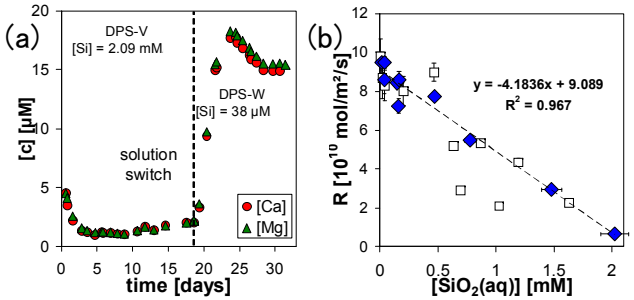
(a)
DPS-V
[Si] = 2.09 mM
DPS-W
[Si] = 38 µM
solution
switch
[Ca]
[Mg]
[c] [µM]
time [days]
(b)
y = -4.1836x + 9.089
R² = 0.967
R [10¹⁰ mol/m²/s]
[SiO₂(aq)] [mM]

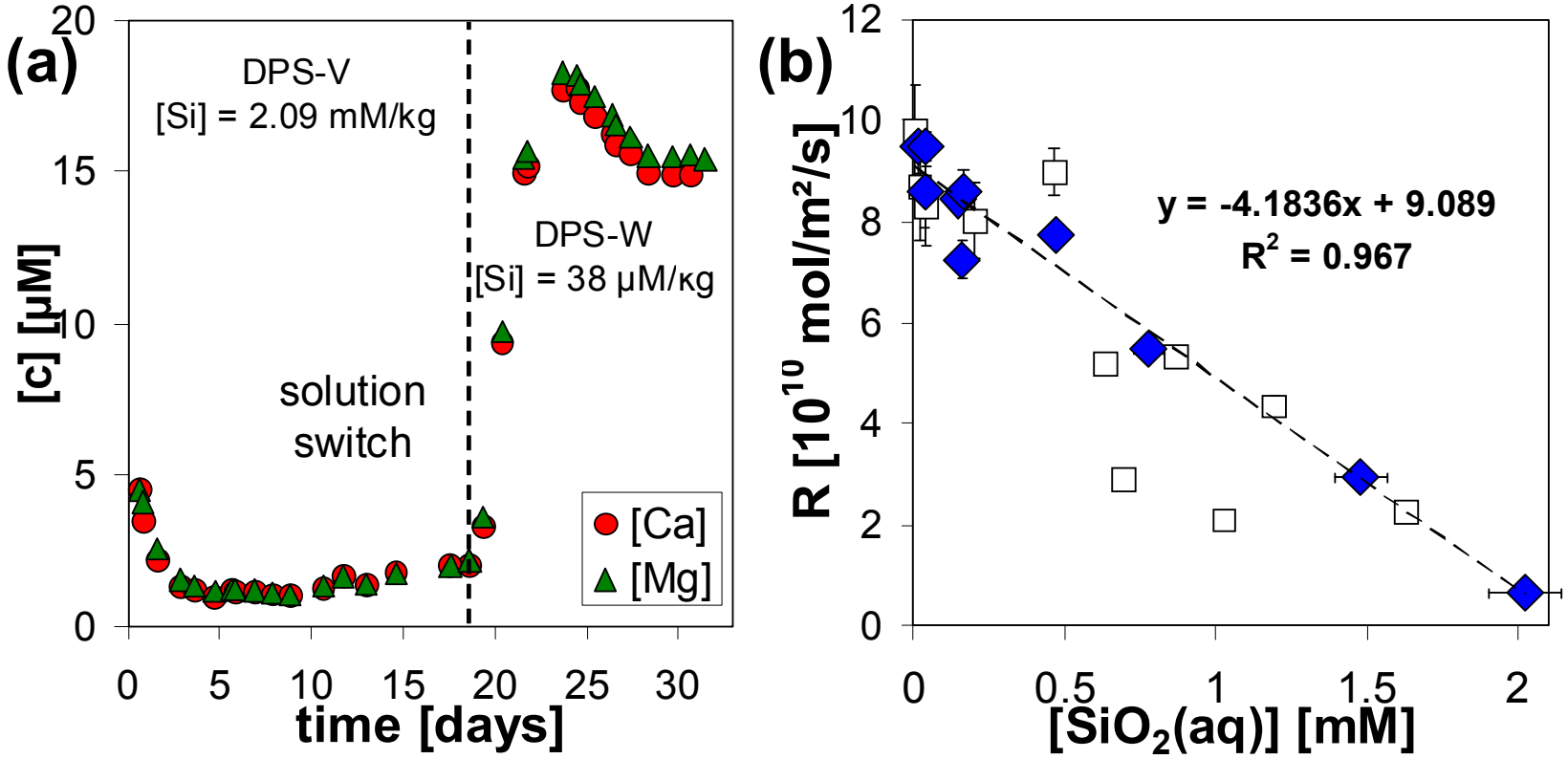
(a)
DPS-V
[Si] = 2.09 mM/kg
DPS-W
[Si] = 38 µM/kg
solution
switch
[Ca]
[Mg]
[c] [µM]
time [days]
(b)
y = -4.1836x + 9.089
R² = 0.967
R [10¹⁰ mol/m²/s]
[SiO₂(aq)] [mM]

Figure 3

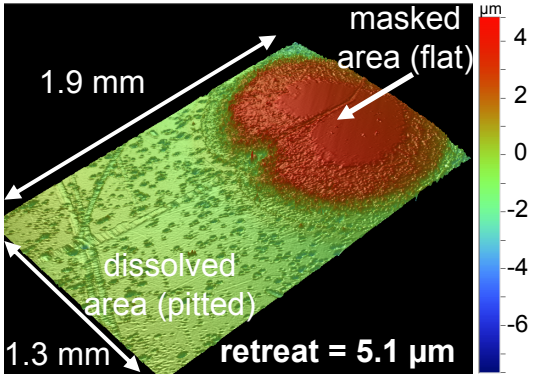
masked
area (flat)
1.9 mm
dissolved
area (pitted)
1.3 mm
retreat = 5.1 µm
µm
4
2
0
-2
-4
-6

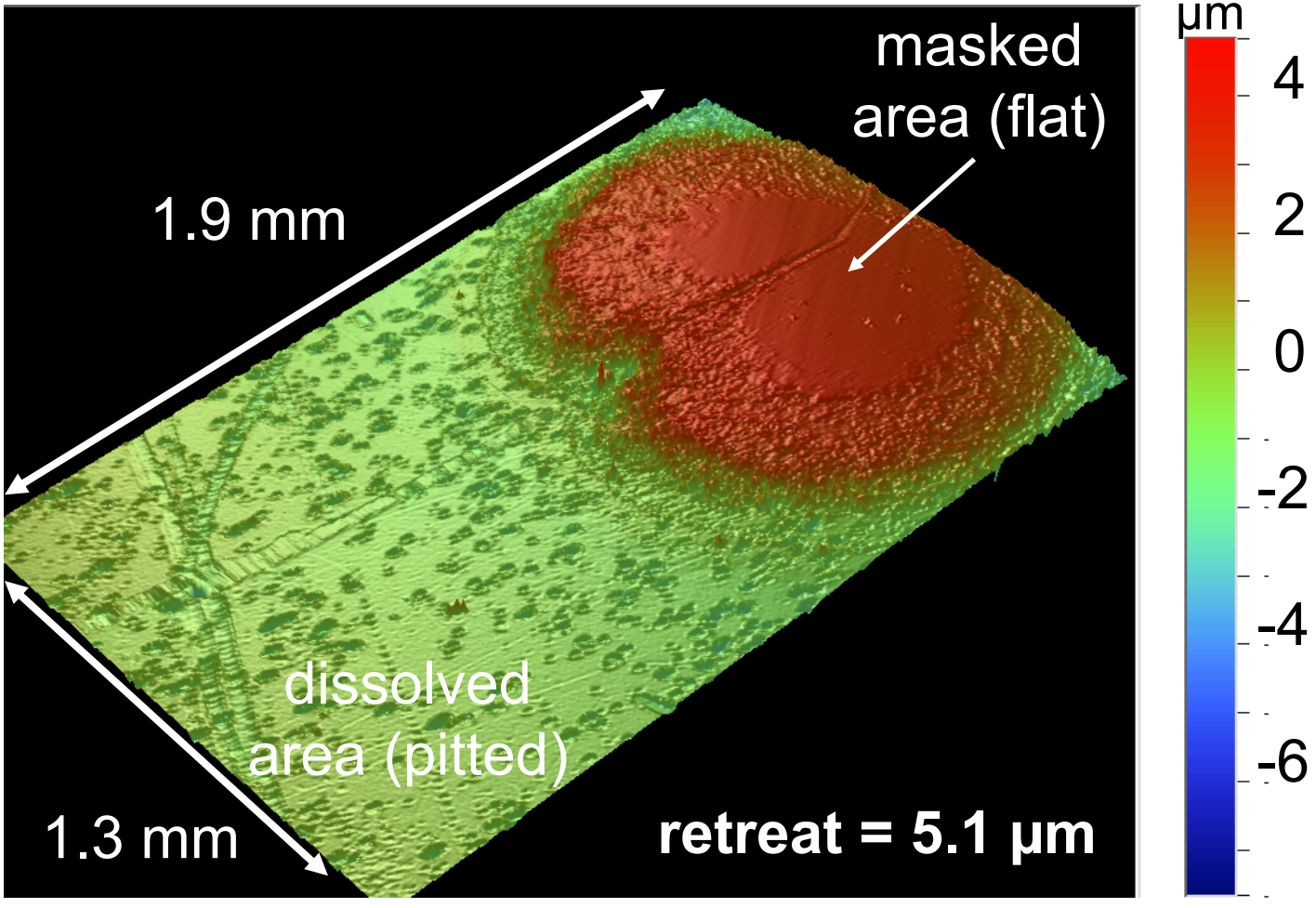
masked
area (flat)
1.9 mm
dissolved
area (pitted)
1.3 mm
retreat = 5.1 µm
µm
4
2
0
-2
-4
-6

Figure 4

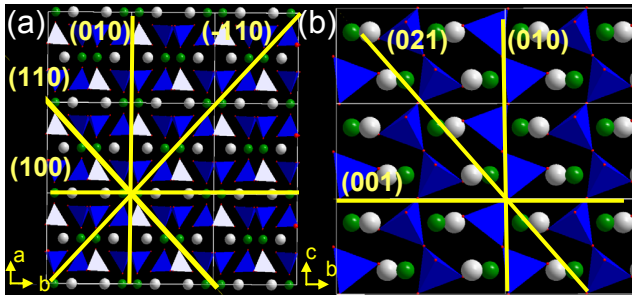
(a)
(010)
(-110)
(110)
(100)
a
b
(b)
(021)
(010)
(001)
c
b

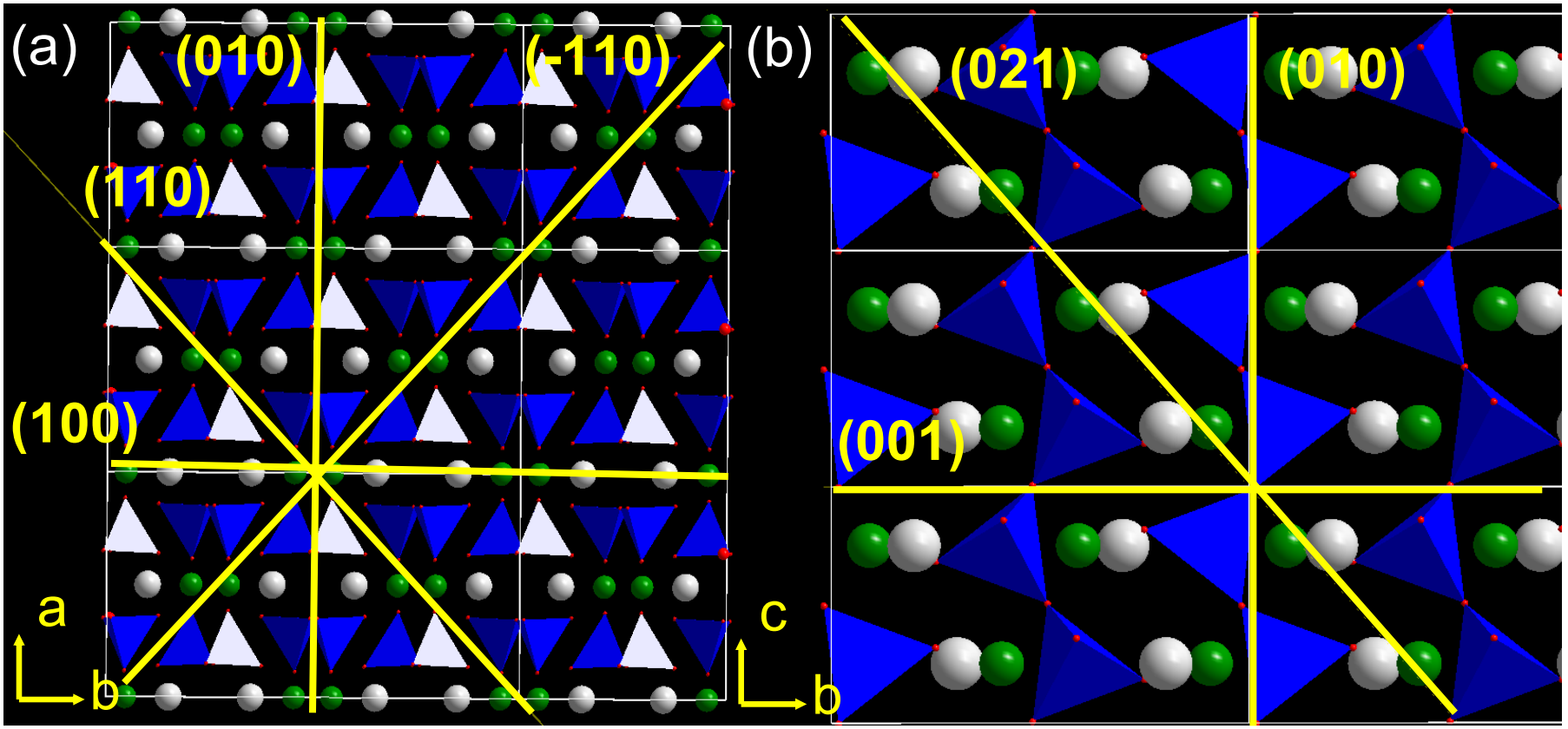
(a)
(010)
(-110)
(110)
(100)
a
b
(b)
(021)
(010)
(001)
c
b

Figure 5

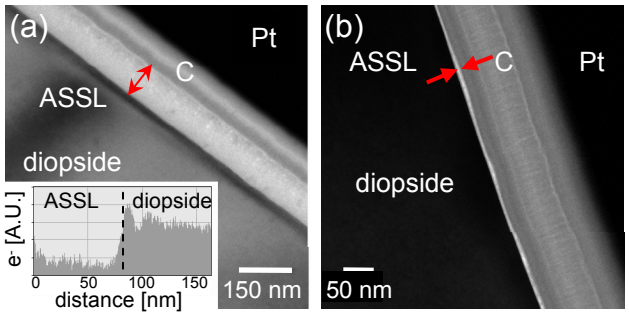
(a)
Pt
C
ASSL
diopside
ASSL
diopside
e- [A.U.]
0
50
100
150
distance [nm]
150 nm
(b)
ASSL
C
Pt
diopside
50 nm

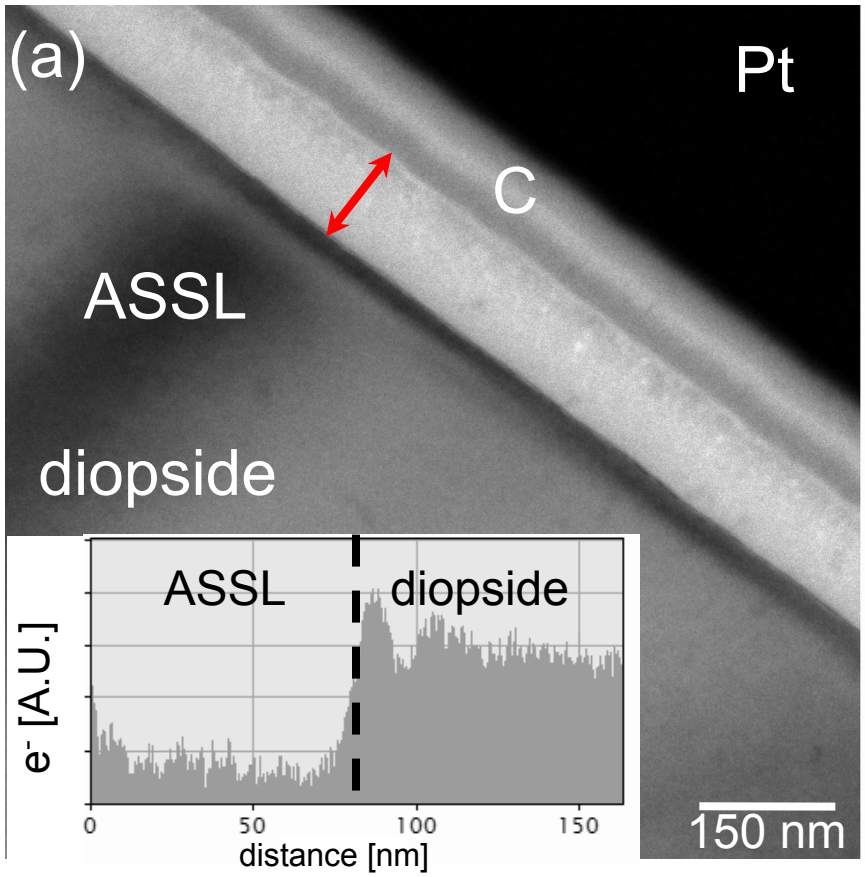
(a)
Pt
C
ASSL
diopside
ASSL
diopside
e- [A.U.]
0
50
100
150
distance [nm]
150 nm

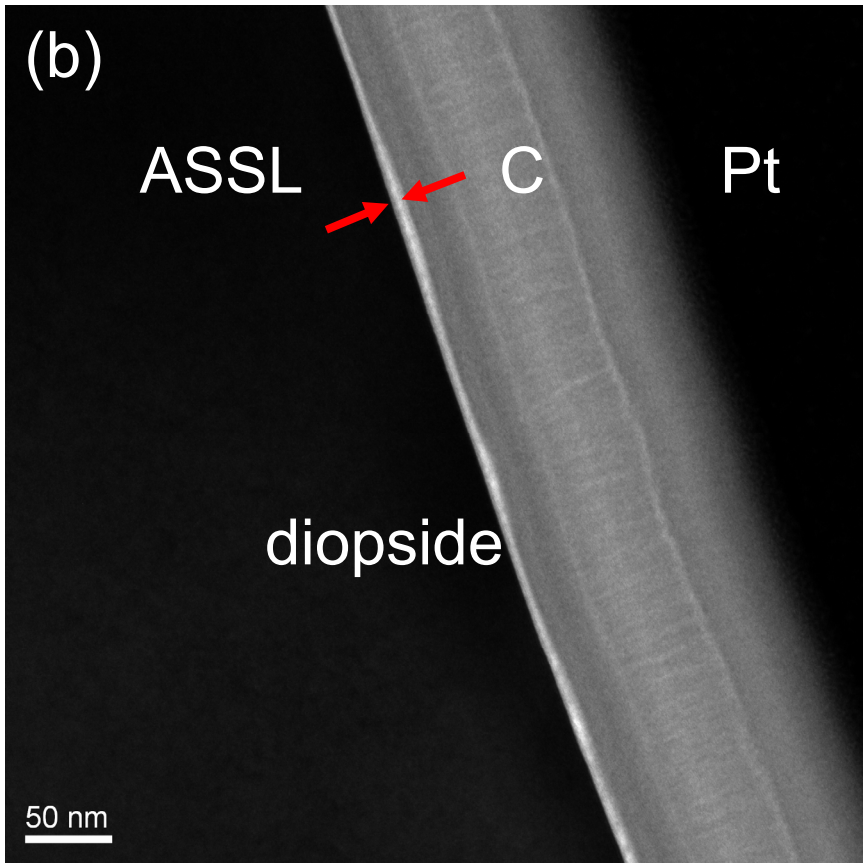
(b)
ASSL
C
Pt
diopside
50 nm

Figure 6

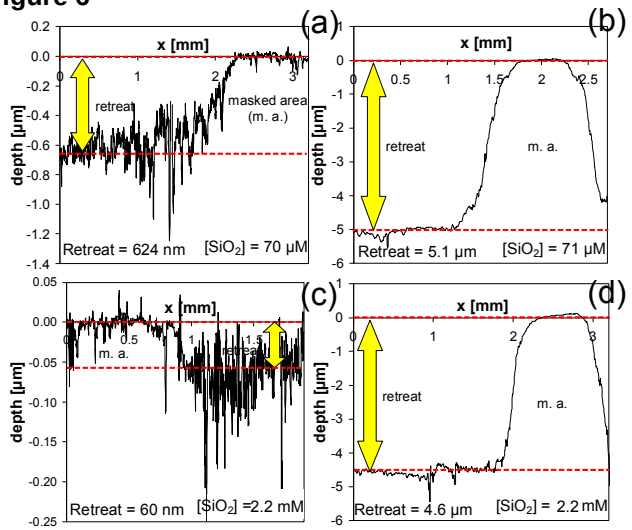
(a)
x [mm]
depth [µm]
retreat
masked area
(m. a.)
Retreat = 624 nm
[SiO2] = 70 µM
(b)
x [mm]
depth [µm]
retreat
m. a.
Retreat = 5.1 µm
[SiO2] = 71 µM
(c)
x [mm]
depth [µm]
m. a.
retreat
Retreat = 60 nm
[SiO2] =2.2 mM
(d)
x [mm]
depth [µm]
retreat
m. a.
Retreat = 4.6 µm
[SiO2] = 2.2 mM

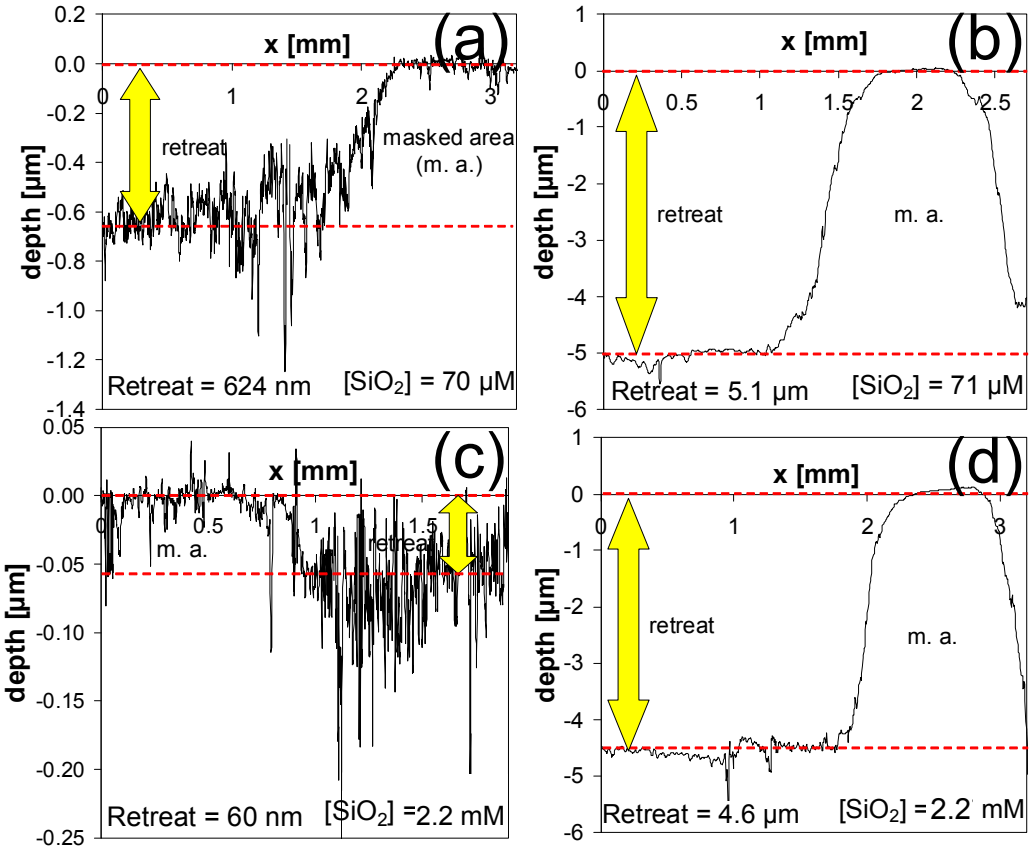
(a)
x [mm]
depth [µm]
retreat
masked area
(m. a.)
Retreat = 624 nm
[SiO2] = 70 µM
(b)
x [mm]
depth [µm]
retreat
m. a.
Retreat = 5.1 µm
[SiO2] = 71 µM
(c)
x [mm]
depth [µm]
m. a.
retreat
Retreat = 60 nm
[SiO2] =2.2 mM
(d)
x [mm]
depth [µm]
retreat
m. a.
Retreat = 4.6 µm
[SiO2] =2.2 mM

Figure 7

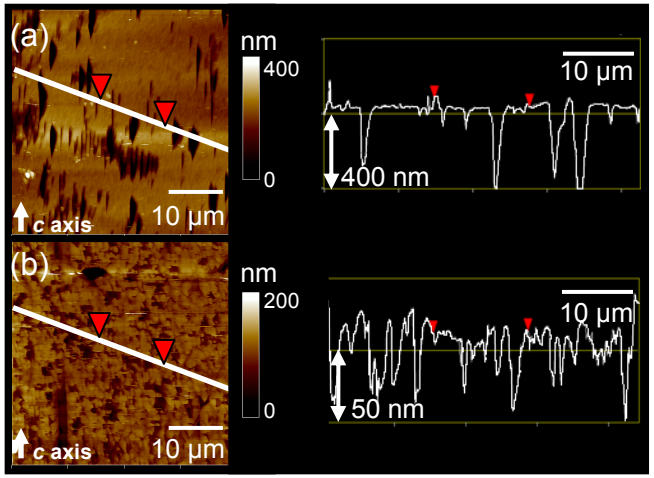
(a)
nm
400
0
10 μm
400 nm
c axis
10 μm
(b)
nm
200
0
10 μm
50 nm
c axis
10 μm

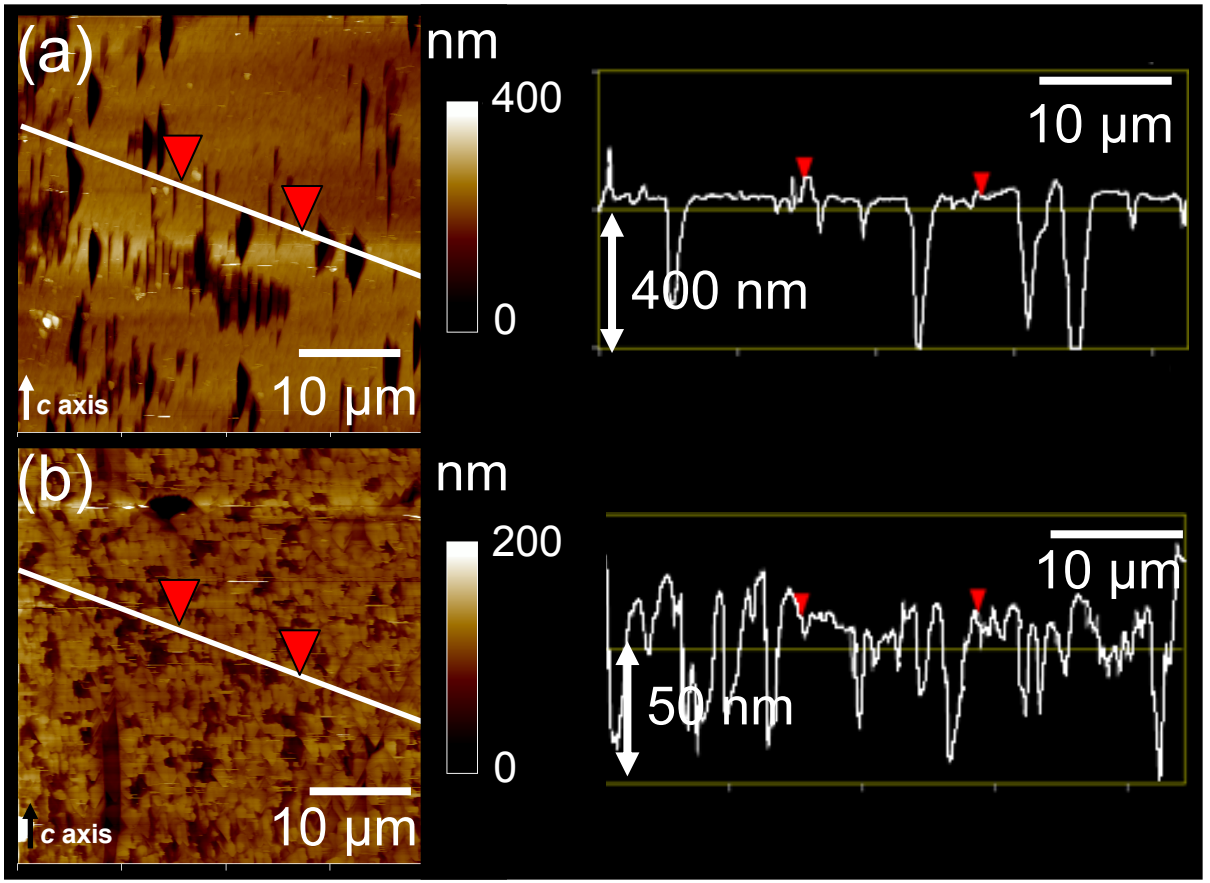
(a)
nm
400
0
10 μm
400 nm
c axis
10 μm
(b)
nm
200
0
10 μm
50 nm
c axis
10 μm

Figure 8

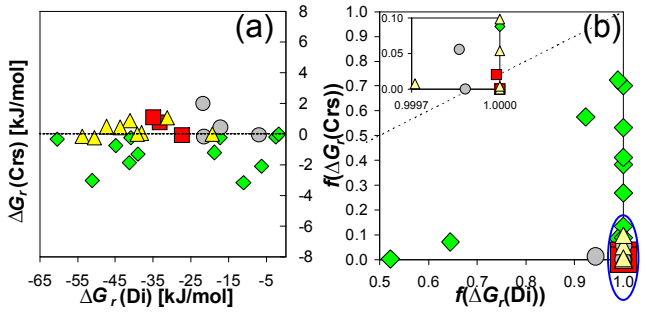
(a)
(b)
ΔGr(Crs) [kJ/mol]
ΔGr(Di) [kJ/mol]
f(ΔGr(Crs))
f(ΔGr(Di))
0.9997
1.0000

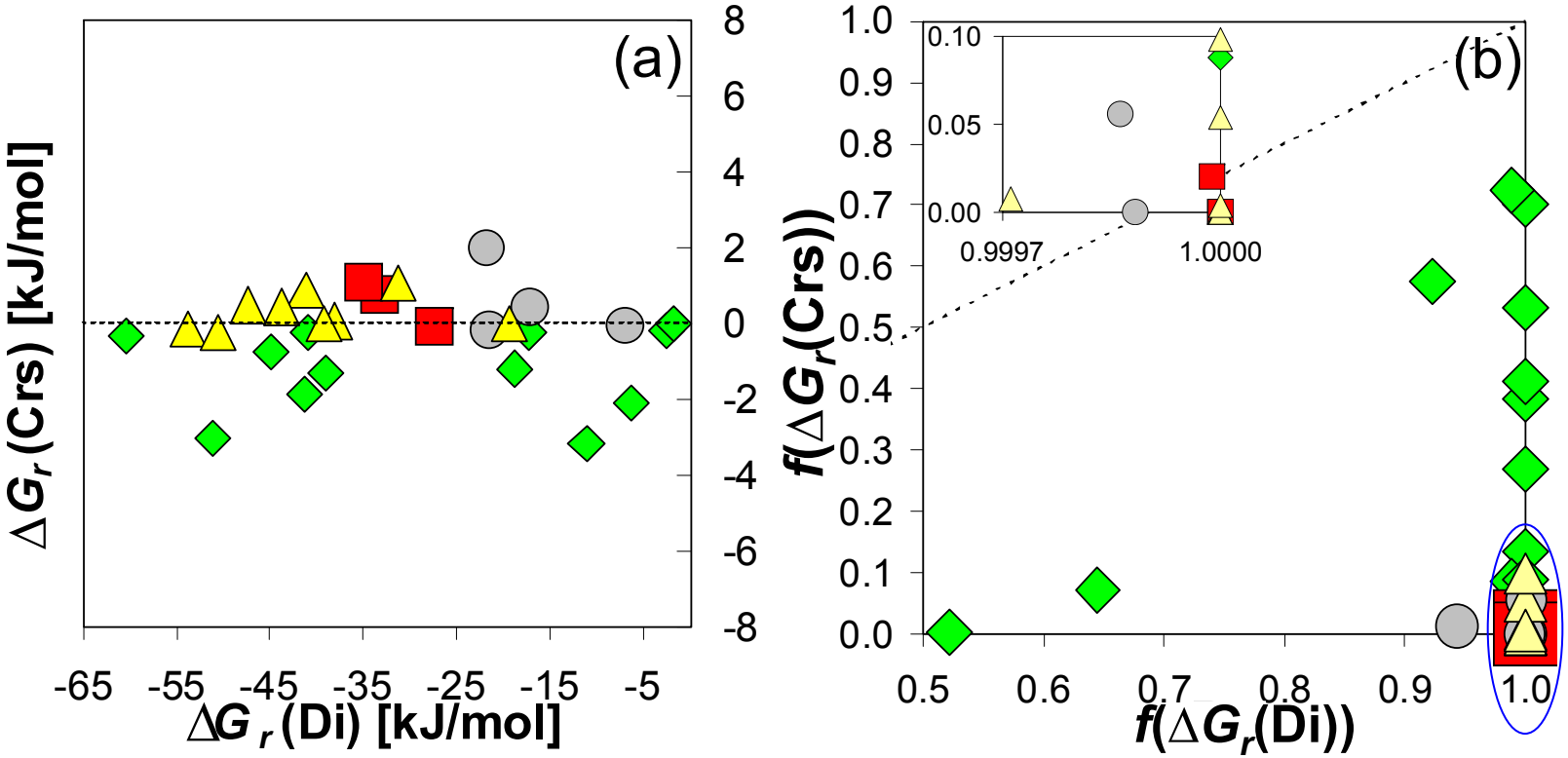
(a)
(b)
ΔGr(Crs) [kJ/mol]
ΔGr(Di) [kJ/mol]
f(ΔGr(Crs))
f(ΔGr(Di))
0.9997
1.0000

Electronic Annex – Supporting information

Fig. EA1. Typical deflection AFM images of diopside reacted in Si-free solutions for 30 days, shown in terms of increasing measured dissolution rates. For each face, a typical pit-volume density ($PVD_{\text{low-Si}}^{(hkl)}$ [$\mu m^3/\ \mu m^2$]) was calculated by cumulating the volume of pits (μm^3) on a given surface area of diopside (μm^2) (averaged over 3 to 6 different images from different locations on the surface). The resulting *PVD* is reported at the top right corner of each image; note that the *PVD* is a convolution of pit density and dimensions. The scale bar in each image represents a distance of 10 µm.

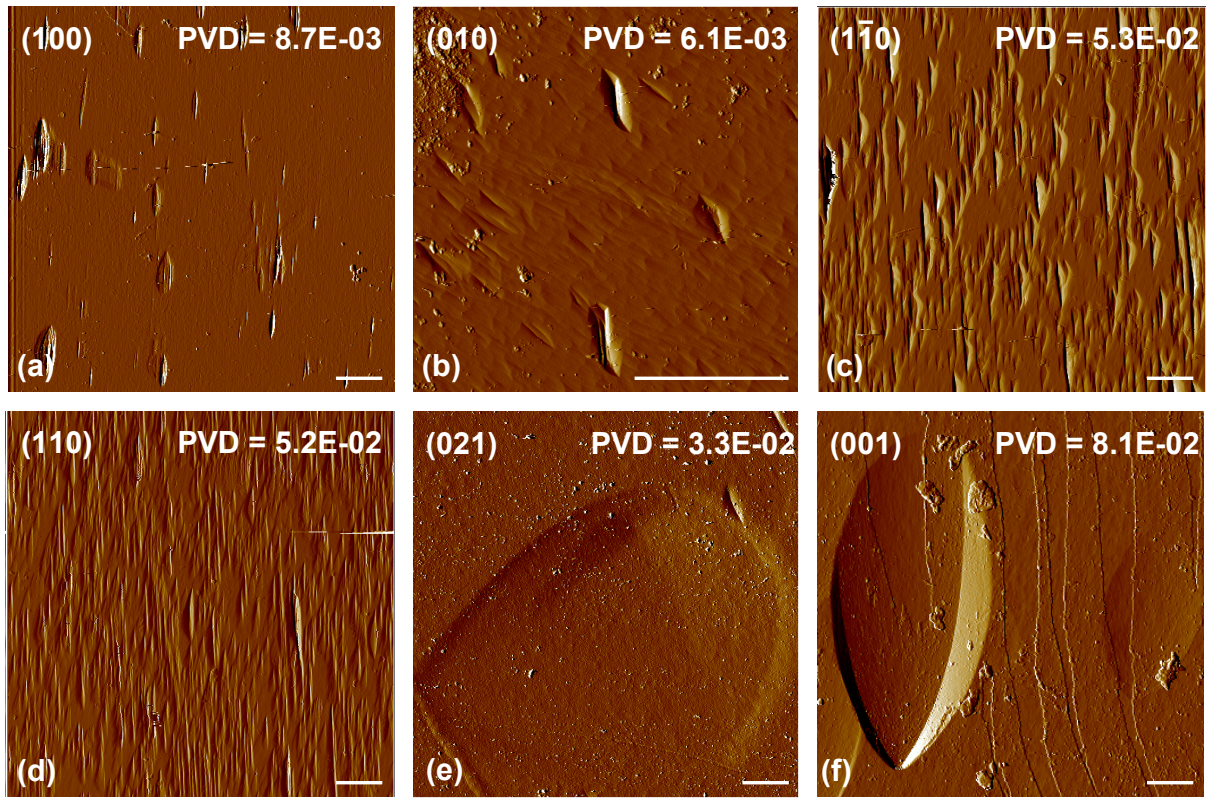

Fig. EA2. HRTEM image of the fluid/diopside interface realized on a FIB-prepared ultrathin section perpendicular to the (110) face after chemical weathering in a Si-rich solution. An amorphous silica rich surface layer (ASSL) formed on the diopside surface, with a mean thickness of ~8 nm. This thickness is equivalent to the ASSL thickness reported for the same face in a Si-free solution.

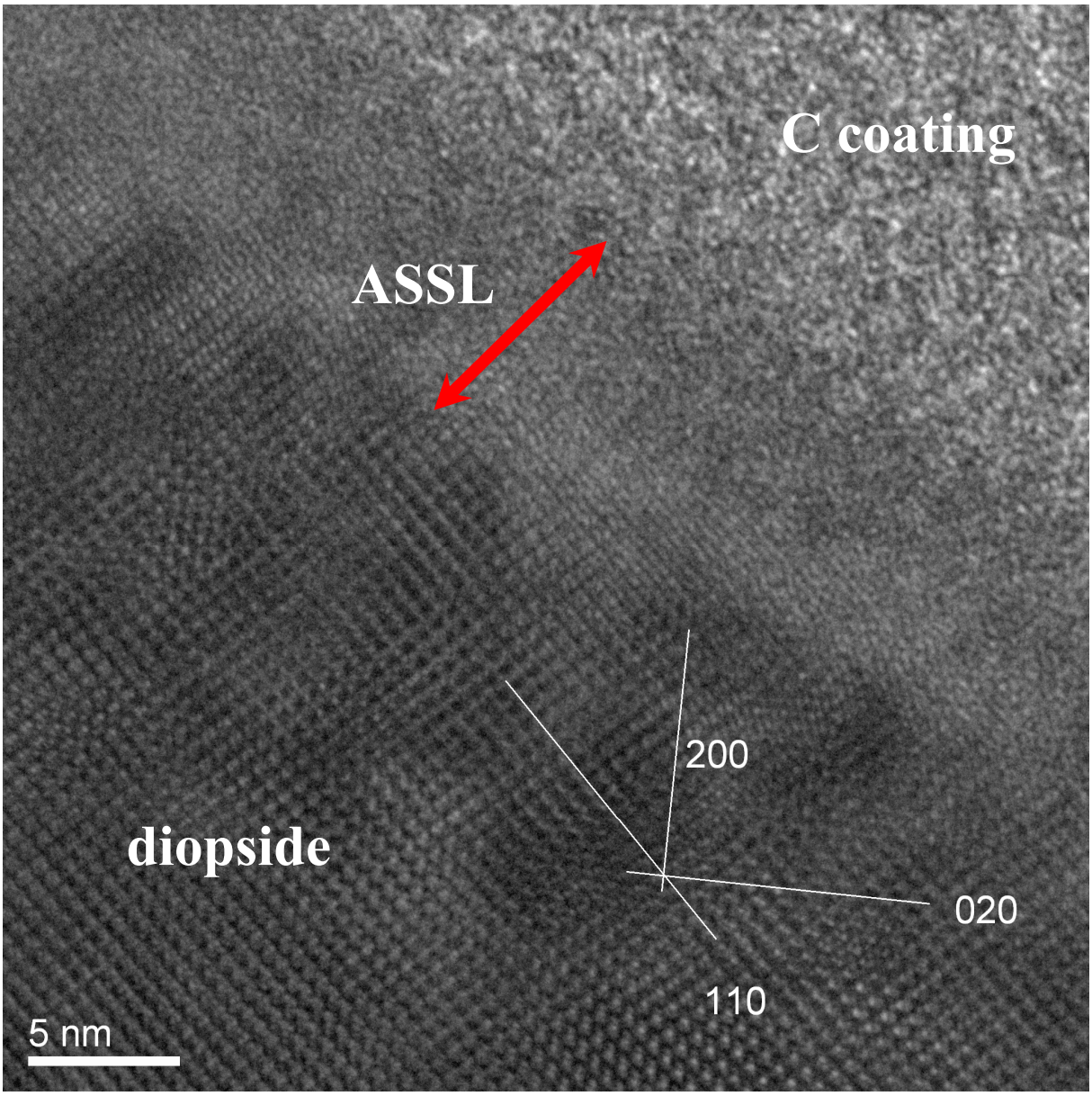

Fig. EA3. Representation of an "ideal" crystal habit of euhedral diopside, and of the expected "ideal" morphology of crushed diopside crystals. Because (110) is the dominant cleavage plane, one can expect that a diopside powder is mainly comprised of grains with (110) (and equivalent $(\bar{1}\bar{1}0)$, $(1\bar{1}0)$ and $(\bar{1}10)$) planes. Because diopside is an inosilicate with silicate chains paralleling the *c* axis, crystals are often elongated in this direction, with a minor contribution of (*hkl*≠0) faces to the total surface area of a grain.

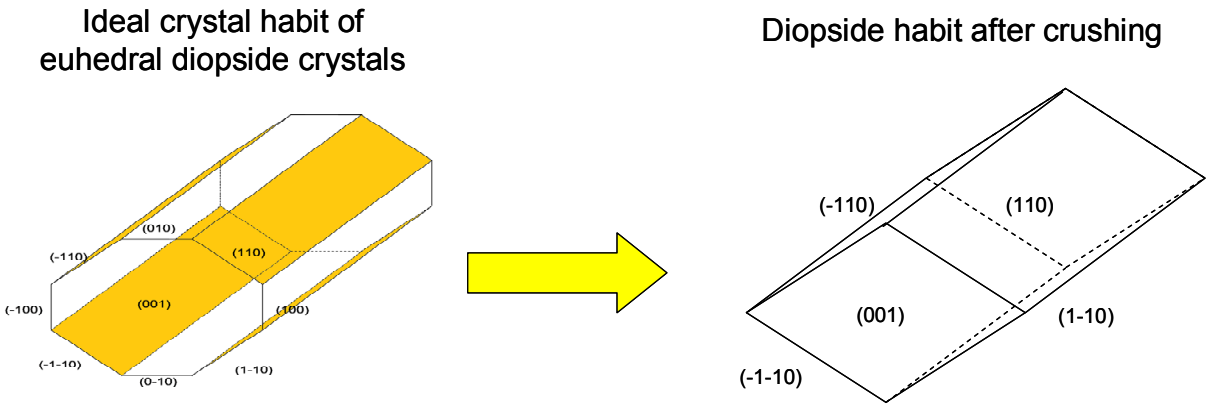

Fig. EA4. HRTEM image of the fluid/diopside interface realized on a FIB-prepared ultrathin section perpendicular to the (021) face after chemical weathering in a Si-poor solution. The amorphous nature of the surface layer is clearly visible.